CM^2 Magazine

第 133 期

南方科技大学海洋磁学中心主编

https://cm2.sustech.edu.cn/

创刊词

海洋是生命的摇篮，是文明的纽带。地球上最早的生命诞生于海洋，海洋里的生命最终进化成了人类，人类的文化融合又通过海洋得以实现。人因海而兴。

人类对海洋的探索从未停止。从远古时代美丽的神话传说，到麦哲伦的全球航行，再到现代对大洋的科学钻探计划，海洋逐渐从人类敬畏崇拜幻想的精神寄托演变成可以开发利用与科学研究的客观存在。其中，上个世纪与太空探索同步发展的大洋科学钻探计划将人类对海洋的认知推向了崭新的纬度：深海（deep sea）与深时（deep time）。大洋钻探计划让人类知道，奔流不息的大海之下，埋藏的却是亿万年的地球历史。它们记录了地球板块的运动，从而使板块构造学说得到证实；它们记录了地球环境的演变，从而让古海洋学方兴未艾。

在探索海洋的悠久历史中，从大航海时代的导航，到大洋钻探计划中不可或缺的磁性地层学，磁学发挥了不可替代的作用。这不是偶然，因为从微观到宏观，磁性是最基本的物理属性之一，可以说，万物皆有磁性。基于课题组的学科背景和对海洋的理解，我们对海洋的探索以磁学为主要手段，海洋磁学中心因此而生。

海洋磁学中心，简称 CM^2，一为其全名“Centre for Marine Magnetism”的缩写，另者恰与爱因斯坦著名的质能方程 $E = MC^2$ 对称，借以表达我们对科学巨匠的敬仰和对科学的不懈追求。

然而科学从来不是单打独斗的产物。我们以磁学为研究海洋的主攻利器，但绝不仅限于磁学。凡与磁学相关的领域均是我们关注的重点。为了跟踪反映国内外地球科学特别是与磁学有关的地球科学领域的最新研究进展，海洋磁学中心特地主办 CM^2 Magazine，以期与各位地球科学工作者相互交流学习、合作共进！

“海洋孕育了生命，联通了世界，促进了发展”。21 世纪是海洋科学的时代，由陆向海，让我们携手迈进中国海洋科学的黄金时代。

目 录

1. 稳定的南半球西风带在全新世最后两千年间开始增强

翻译人：仲义 zhongy@sustech.edu.cn

Van der Bilt, W., D'Andrea, W.J., Oppedal, L. T., ***Stable Southern Hemisphere westerly winds throughout the Holocene until intensification in the last two millennia*** *[J] Communications Earth & Environment, 2022, 49(16), e2022GL099772.*

https://doi.org/10.1038/s43247-022-00512-82

摘要：南半球的西风带维持着南大洋作为地球主要的碳汇，并帮助封存了近一半的人为产生的二氧化碳进入海洋当中。观测结果显示，这一气候调节器的动力发生了变化，但由于缺乏基线数据的支持，模型无法预估未来气候变化影响碳储量。本文中作者利用沉积脂质的氢同位素比值来解析南半球西风带强度变化。重建结果显示直到 2150 年达到稳定值，且化合物更加富氢。作者将这种同位素漂移归因于西风驱动的湖泊水分蒸发，而区域性古气候证据表明，它标志着一种向南大洋主要大气模态向负南大洋环状模态转变的趋势。由于这种变化在过去 7000 年里是无法匹配的，作者的研究结果表明，之前已发表的用于衡量未来变化的千年尺度南半球环状模态指数可能无法捕捉到自然变化的全部范围。

ABSTRACT: The Southern Hemisphere westerly winds sustain the Southern Ocean's role as one of Earth's main carbon sinks, and have helped sequester nearly half the anthropogenic CO2 stored in the ocean. Observations show shifts in the vigor of this climate regulator, but models disagree how future change impacts carbon storage due to scarce baseline data. Here, we use the hydrogen isotope ratios of sedimentary lipids to resolve Holocene changes in Southern Hemisphere westerly wind strength. Our reconstruction reveals stable values until ~2150 years ago when aquatic compounds became more 2H-enriched. We attribute this isotope excursion to wind-driven lake water evaporation, and regional paleoclimate evidence shows it marks a trend towards a negative Southern Annular Mode – the Southern Ocean's main mode of atmospheric variability. Because this shift is unmatched in the past 7000 years, our findings suggest that previously published millennium-long Southern Annular Mode indices used to benchmark future change may not capture the full range of natural variability.

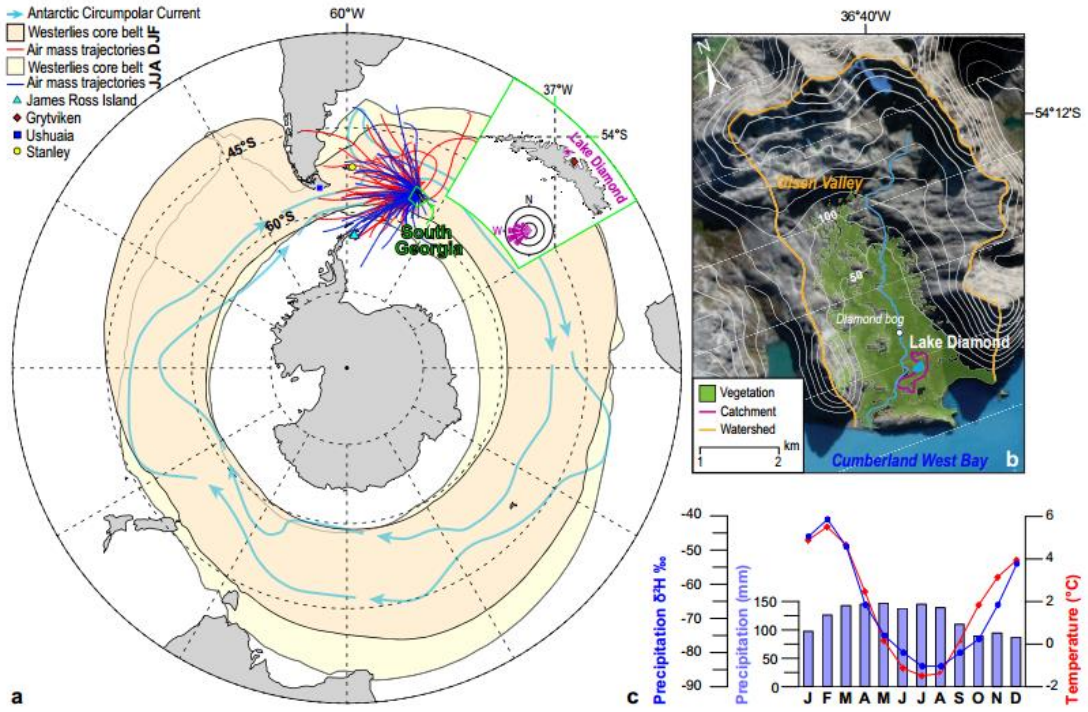

Figure 1. Key localities and observations. a Overview map of the Southern Ocean with an inset of South Georgia, highlighting Lake Diamond as well as the nearest weather stations of Grytviken, Ushuaia, and Stanley in color coding that corresponds with Fig. 2. The average position and extent of the Southern Westerlies core belt, defined as areas where mean zonal wind speeds exceed 5 m/s−1 between 1981–2010 CE122, is shown for the Austral summer (DJF) and winter (JJA). The purple wind rose shows the prevalence of this dominant wind system. Forty-eight hours daily backward air mass trajectories from 2019 are shown for summer (red) and winter (blue). The long-term position of the Antarctic Circumpolar Current (ACC) is delimited in cyan by the Antarctic convergence to the South and the Sub-Antarctic front to the North after124. b Close-up of the Lake Diamond catchment and the wider Olsen valley as modified after29. Vegetated areas, defined as surfaces with normalized difference vegetation index (NDVI) values >0.3 during the growing season (January 2020)33, are highlighted in green. Sentinel-2 satellite image courtesy of the ESA Copernicus Open Access Hub. c Long-term monthly local climatology based on 1905-2012 CE station data from nearby Grytviken23 and spatial δ2H interpolation.

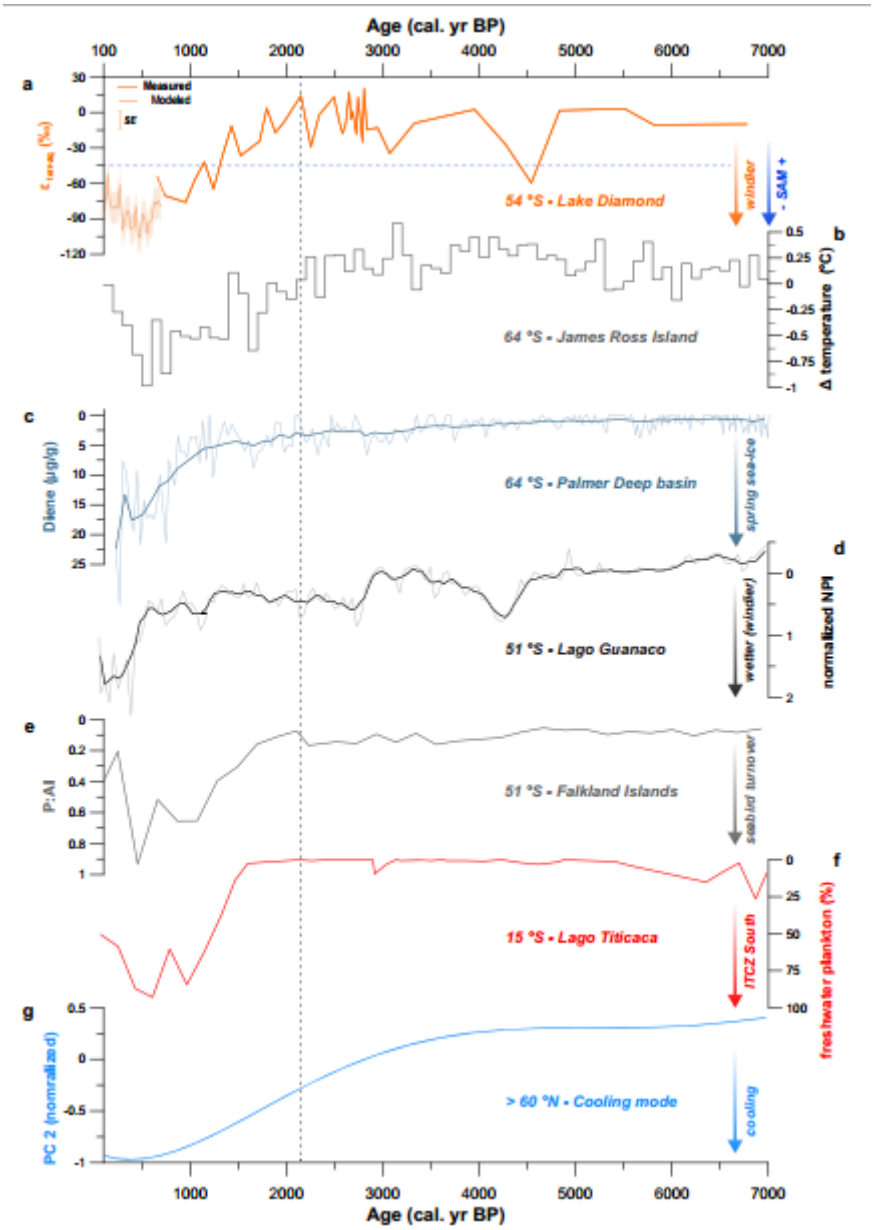

Figure 2. Comparing evaporation in Lake Diamond with regional proxies of sea ice, wind, seabird, and temperature shifts. a Lake Diamond εterr-aq values. Please note that we distinguish between reconstructed and PTP-inferred values (see methods), while also displaying the SE of this model. b James Ross Island (JRI) ice core temperature reconstruction after44, showing 100-year averaged anomalies compared to the CE 1961–1990 mean. c Diatom-derived diunsaturated (diene) highly branched isoprenoid (HBI) biomarker concentrations from81. d Raw and smoothed standardized Nothofagus (southern beech tree)/Poaceae (grass) Index (NPI) values from40. e Seabird-derived ratios of bio-element Phosphorus (P) over lithogenic Aluminum (Al) after82. f Freshwater plankton abundances (%) in Lake Titicaca from104. g Normalized smoothed principal component 2 (PC2) values of the global cooling mode inferred by ref. 109.

2. 尽管大气 CO2 含量下降，但始新世出现了高度钙化的球状石藻

翻译人：蒋晓东 jiangxd@sustech.edu.cn

Claxton L M, McClelland H L O, Hermoso M et al. ***Eocene emergence of highly calcifying coccolithophores despite declining atmospheric CO_2*** *[J]. Nature Geoscience, (2022)*
https://doi.org/10.1038/s41561-022-01006-0

摘要：球状石藻是一组单细胞钙化浮游植物，是海洋碳酸盐生产的主要贡献者，因为它们产生的方解石板片(球石)首次出现在 200 百万年前的化石记录中。这一过程在进化时间尺度上对环境变化的响应仍然知之甚少，尤其是在温暖地区气候。在这里，我们整合了一个由海洋沉积物中基于颗粒大小的球石方解石碳同位素比值组成的数据集，用细胞尺度模型来研究过去 100 百万年前内地球上最热的始新世(~ 55-34 Ma)的细胞碳通量和二氧化碳分压。我们发现大型球状石藻在始新世因具有更高的钙化和固碳比而主导海洋沉积，而较小的球石藻则相反。这些变化发生在海洋碱化加剧的背景下，颗石藻钙化在正向碳循环反馈和降低二氧化碳分压中可能发挥了明显作用。基于多指标的证据，我们的方法对于中新世 CO_2 分压随着温度降低还提供了的独立支持。总之，这一工作挑战了新兴观点：二氧化碳分压的普遍下降减少了进化时间尺度上的钙化。

ABSTRACT: Coccolithophores, a group of unicellular calcifying phytoplankton, have been major contributors to marine carbonate production since the calcite plates that they produce (coccoliths) first appeared in the fossil record over 200 million years ago (Ma). The response of this process to changes in environment on evolutionary timescales remains poorly understood, particularly in warm climates. Here we integrate a dataset consisting of carbon isotope ratios of size-separated coccolith calcite from marine sediments with a cell-scale model to interrogate cellular carbon fluxes and pCO_2 through the Eocene (~55–34 Ma), Earth's hottest interval of the past 100 million years. We show that the large coccolithophores that rose to dominate the oceans through the Eocene have higher calcification-to-carbon fixation ratios than their predecessors while the opposite is true for smaller coccolithophores. These changes, which occurred in the context of increasing ocean alkalization, may have played a role in an apparent positive carbon cycle feedback to decreasing pCO_2. Our

approach also provides independent support of multiproxy-based evidence for general pCO_2 decline through the Eocene in step with temperature. Together, this challenges the emerging view that a general decline in pCO_2 reduces calcification on evolutionary timescales.

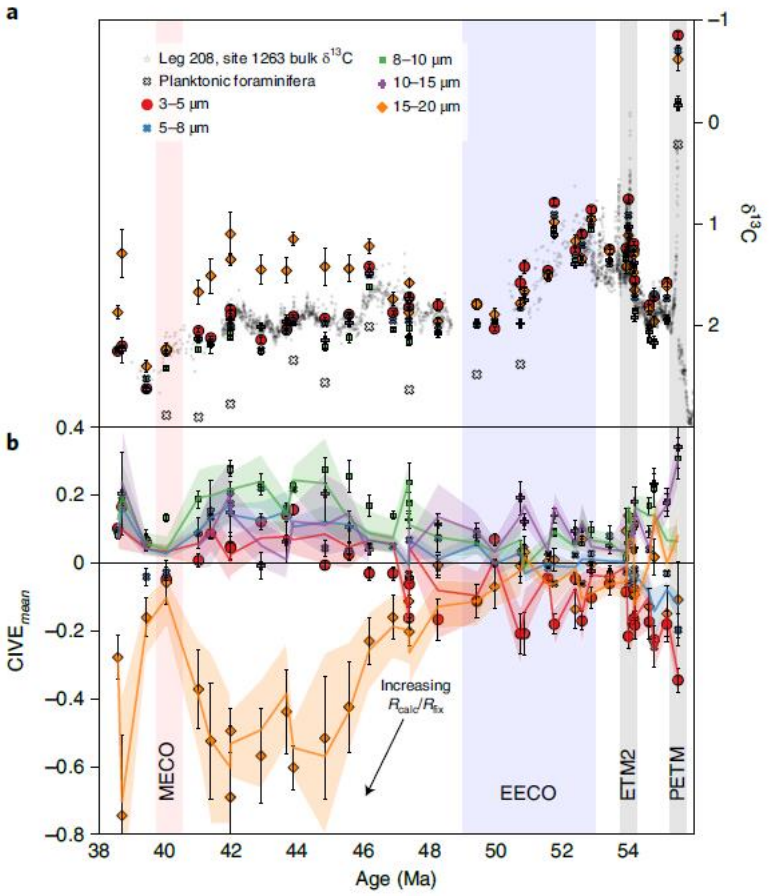

Figure 1. Modelled versus measured CIVEmean. a, Measured $\delta^{13}C$ across all five size fractions and coeval foraminifera measurements. Coeval foraminifera are composed of the genus Acarinina, which probably had symbionts, hence leaving the foraminifera calcite enriched in ^{13}C; we investigate vital effects associated with foraminifera in the Supplementary Information. Also shown are contemporaneous bulk sediment $\delta^{13}C$ values, which track the total sum of coccolith and foraminifera calcite and changes depending on their proportion, vital effects and mixed-layer whole-ocean signals. Covariation between the fine fractions and bulk is interpreted to imply that the bulk is largely composed of coccoliths and so their calcite dominates the geochemistry, although we cannot rule out some overgrowth (Supplementary Information). b, $\delta^{13}C$ values of each sediment size fraction relative to their age interval mean (CIVEmean). Points are measurements; lines are fitted model values. The error bars on the points represent uncertainty introduced through contamination of neighbouring size fractions (Methods). The coloured envelope surrounding each line represents 95% of model runs over 10,000 Monte Carlo simulations. The coloured vertical regions represent important periods during the Eocene, including the Palaeocene–Eocene Thermal Maximum (PETM), ETM2, early Eocene Climatic Optimum (EECO) and MECO.

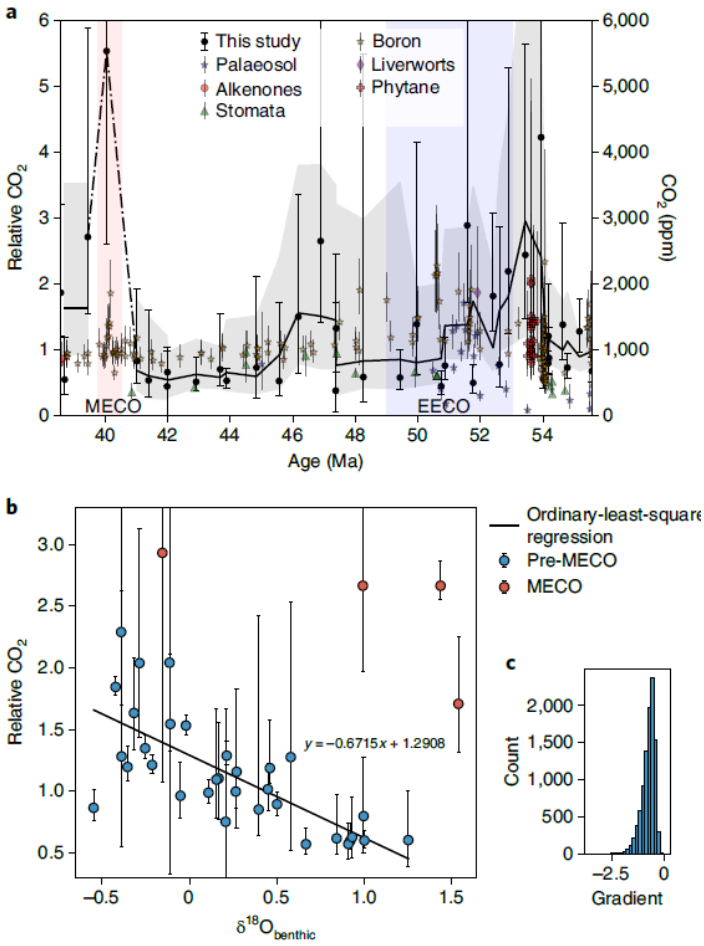

Figure 2. Relative CO2 change through the Eocene. a, Relative CO2, defined as model output CO2 (aq) relative to model input CO2, is derived from our optimized model with size-differentiated isotopic constraints (see Methods for detailed explanation of relative CO2). The coloured markers represent previously published p CO2 data across the Eocene (right-hand y axis). The black circles represent the median relative CO2 (aq) over 10,000 iterations of our Monte Carlo optimization (left-hand y axis), with error bars representing plus and minus 2-sigma of all realisations for each age point (95% of realizations). The black line represents a three-point moving average of our output, with the grey shaded region representing the moving average of plus 2 sigma and minus 2 sigma. Our modelled low relative CO2(aq) during the middle Eocene coincides with a step-wise increase in proxies linked to an increase in the rate of chemical weathering and therefore CO2 draw-down. The dashed black line during the MECO joins points without a moving average. Using a moving average at this time greatly skews the trend line given the large, and uncertain, deviation to higher relative CO2. Also shown is the approximate interval of the EECO. b, The five-point moving average of relative CO2(aq) is plotted against the five-point moving average of δ18Obenthic. The five-point moving average was used to avoid noise in the data and evaluate the longer-term trend. Error bars represent one sigma uncertainty on reconstructed CO2(aq) values. The equation of the line has been overlaid on the figure. The four points in red represent the points from the MECO and younger, which have been excluded from the P-value calculation ($P < 0.001$). Without the MECO data included, our relative e (aq) and δ18Obenthic show a robust negative correlation. The warmer early Eocene, characterized by more negative values of δ18Obenthic, has on average higher values of relative CO2(aq). c, The slope of relative e (aq) with δ18Obenthic for each of the 10,000 Monte Carlo simulations was calculated and plotted as a histogram. Only one value was greater than zero.

3. EPICA Dome C（EDC）冰心高分辨率水同位素记录中的亚千年尺度气候变化

翻译人：盖聪聪 gaicc@sustech.edu.cn

Grisart A, Casado M, Gkinis V, et al. ***Sub-millennial climate variability from high-resolution water isotopes in the EPICA Dome C ice core*** *[J]. Climate of the Past, 2022, 18, 2289-2301.*
https://doi.org/10.5194/cp-18-2289-2022

摘要：EPICA Dome C（EDC）冰芯提供了最长的、覆盖了过去 80 万年的连续气候记录，其高分辨率水同位素（$\delta^{18}O$ 和δD）记录为研究过去冰期和间冰期的年代际到千年际的变化提供了独特的机会。我们在 11 cm 的采样分辨率下汇编了 EDC 水同位素的连续记录，共 27000 个$\delta^{18}O$ 以及 7920 个δD 数据（分别覆盖整个 EDC 记录的 94%和 27%）。其中，过去 800 千年以来的数据包括已发表的、以及新测量的 2900 个$\delta^{18}O$ 和δD 数据。本文证明了对采集于多种深度区间的 EDC 样品而言，不同分析方法获得的同位素数据在分析不确定度范围内具有可比性。因此，我们整合了所有可用的 EDC 水同位素测量结果，建立了过去 800 千年的高分辨率（11 厘米）数据集。对最完整的$\delta^{18}O$ 记录的频率分解、以及对扩散作用的简单评估表明，在年代际到百年际的时间尺度上，冰期的变率高于间冰期，同位素极大值在间冰期高于全新世。这一分析还表明，对于那些温度最适宜发生在早期的间冰期，百年际变率最强发生在温度最适宜期。

ABSTRACT: The EPICA Dome C (EDC) ice core provides the longest continuous climatic record, covering the last 800 000 years (800 kyr). A unique opportunity to investigate decadal to millennial variability during past glacial and interglacial periods is provided by the high-resolution water isotopic record ($\delta^{18}O$ and δD) available for the EDC ice core. We present here a continuous compilation of the EDC water isotopic record at a sample resolution of 11 cm, which consists of 27000 $\delta^{18}O$ measurements and 7920 δD measurements (covering, respectively, 94 % and 27 % of the whole EDC record), including published and new measurements (2900 for both $\delta^{18}O$ and δD) for the last 800 kyr. Here, we demonstrate that repeated water isotope measurements of the same EDC samples from different depth intervals obtained using different analytical methods are

comparable within analytical uncertainty. We thus combine all available EDC water isotope measurements to generate a high-resolution (11 cm) dataset for the past 800 kyr. A frequency decomposition of the most complete $\delta^{18}O$ record and a simple assessment of the possible influence of diffusion on the measured profile shows that the variability at the multi- decadal to multi-centennial timescale is higher during glacial than during interglacial periods and higher during early interglacial isotopic maxima than during the Holocene. This analysis shows as well that during interglacial periods characterized by a temperature optimum at the beginning, the multi- centennial variability is strongest over this temperature optimum.

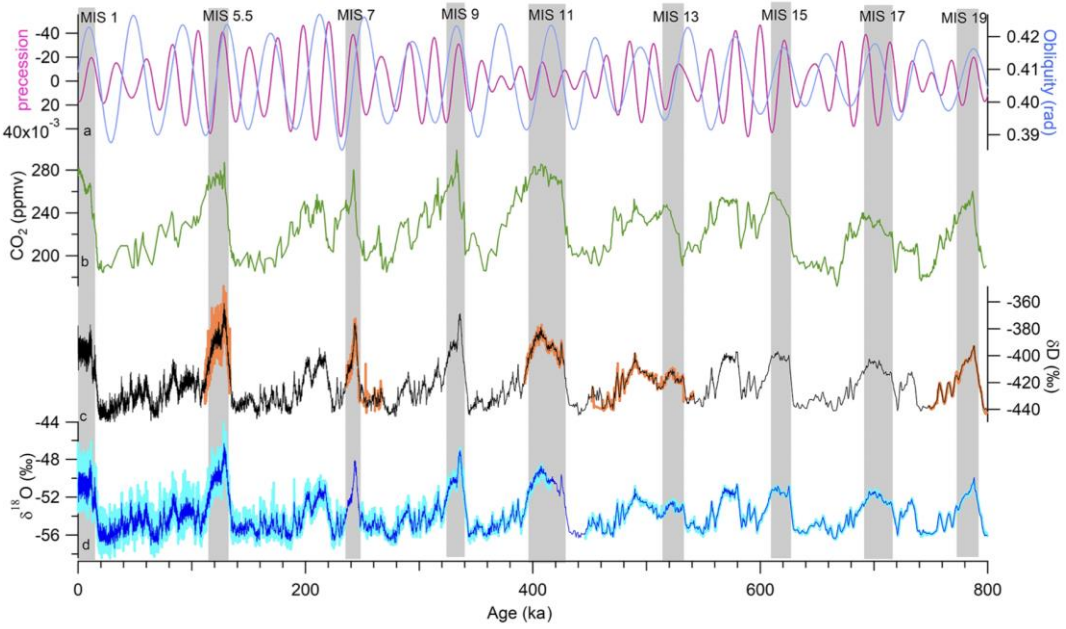

Figure 1. EDC ice core and other palaeoclimate records as well as variations in Milankovitch cycles over the past 800 kyr. (a) Precession (pink) and obliquity (blue); (b) composite EDC and Vostok CO_2 record over the last 800 kyr; (c) the EDC δD record at 11 cm (orange) and 55 cm (black) resolution; and (d) the EDC $\delta^{18}O$ record at 11 cm (light blue) and 55 cm (dark blue) resolution. All ice core records are presented on the AICC2012 scale. Grey rectangles indicate the positions of interglacial periods.

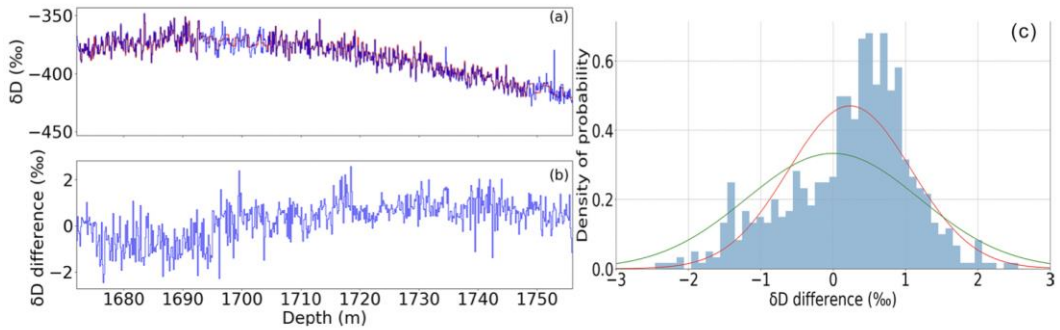

Figure 2. (a) EDC δD measurements versus depth (m) over Termination 2: measurements completed in

2010 at LSCE (uranium reduction method) are shown in blue, and measurements completed in 2019 at LSCE (CRDS method) are shown in red. (b) Difference between the δD values measured in 2010 and 2019. (c) Probability density function for the difference between the first (uranium reduction) and the new (CRDS) δD measurements. A Gaussian curve (red) is fitted to the data. Another Gaussian curve (green) with the standard deviation equal to the classically displayed 1σ uncertainty of δD measurements with the CRDS method at LSCE (1σ = 0.7 ‰) is also displayed.

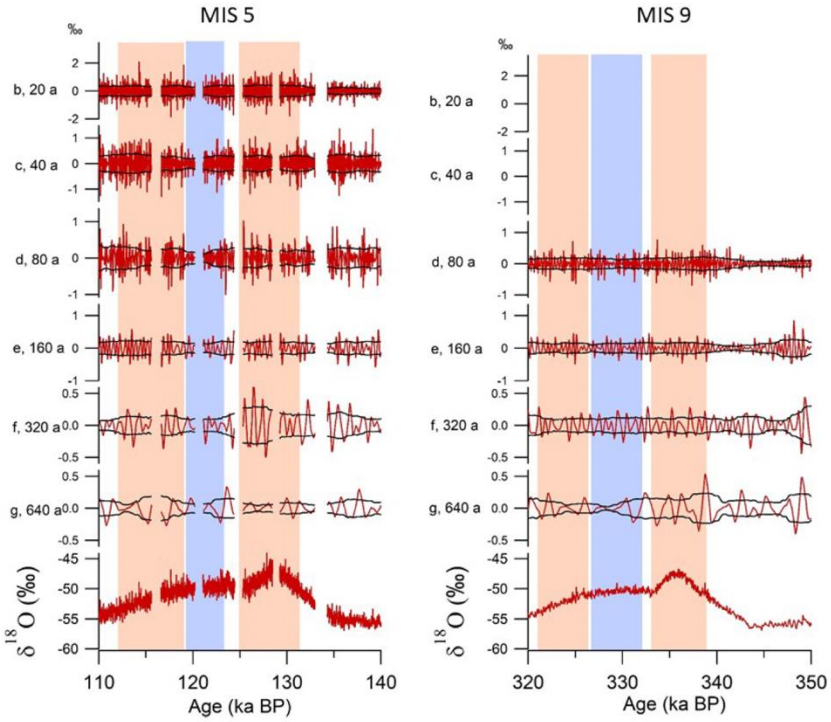

Figure 3. Contributions to the original $\delta^{18}O$ signal (red) of the MRA composites with resolutions of 20 (b), 40 (c), 80 (d), 160 (e), 320 (f) and 640 (g) years for MIS 5 and MIS 9.The black envelope presents the running standard deviation (1σ) in 3 kyr windows. The red rectangles indicate periods with enhanced variability and the blue rectangles indicate periods with reduced variability.

4. 南极横贯山脉 60 个百万年来的冰期

翻译人：张琪 zhangq7@sustech.edu.cn

*Barr L, Spagnolo M, Rea B, et al, **60 million years of glaciation in the Transantarctic Mountains** [J]. Nature Communications, 2022.*
https://doi.org/10.1038/s41467-022-33310-z

摘要：南极大陆在约 83 Ma 到达其目前的极地位置，并被冰盖覆盖约 34 Ma，巧合的是这与始新世-渐新世交界处急剧的全球变冷相一致。然而，南极冰川是在这个时期突然首次出现，还是在更早的时候就出现了，还尚未可知。本文提出，横贯南极山脉的冰川可能在晚古新世（~60-56 Ma）和中始新世（~48-40 Ma）就已经存在。在晚始新世（~40-34 Ma）和渐新世（~34-23 Ma）期间暖冰川普遍存在，在更大的冷冰川（包括冰盖）占主导地位之前，暖冰川数量有所减少。一些暖冰川出现在中新世气候适宜期（~15 Ma），之后便转向广泛存在的冷冰川。本文强调了南极洲冰川的存续时间，并表明甚至在早新生代温室气候期间冰川就已经存在了。

ABSTRACT: The Antarctic continent reached its current polar location ~83 Ma and became shrouded by ice sheets ~34 Ma, coincident with dramatic global cooling at the Eocene-Oligocene boundary. However, it is not known whether the first Antarctic glaciers formed immediately prior to this or were present significantly earlier. Here we show that mountain glaciers were likely present in the Transantarctic Mountains during the Late Palaeocene (~60–56 Ma) and middle Eocene (~48–40 Ma). Temperate (warm-based) glaciers were prevalent during the Late Eocene (~40–34 Ma) and, in reduced numbers, during the Oligocene (~34–23 Ma), before larger, likely cold-based, ice masses (including ice sheets) dominated. Some temperate mountain glaciers were present during the Miocene Climatic Optimum (~15 Ma), before a widespread switch to cold-based glaciation. Our findings highlight the longevity of glaciation in Antarctica and suggest that glaciers were present even during the Early-Cenozoic greenhouse world.

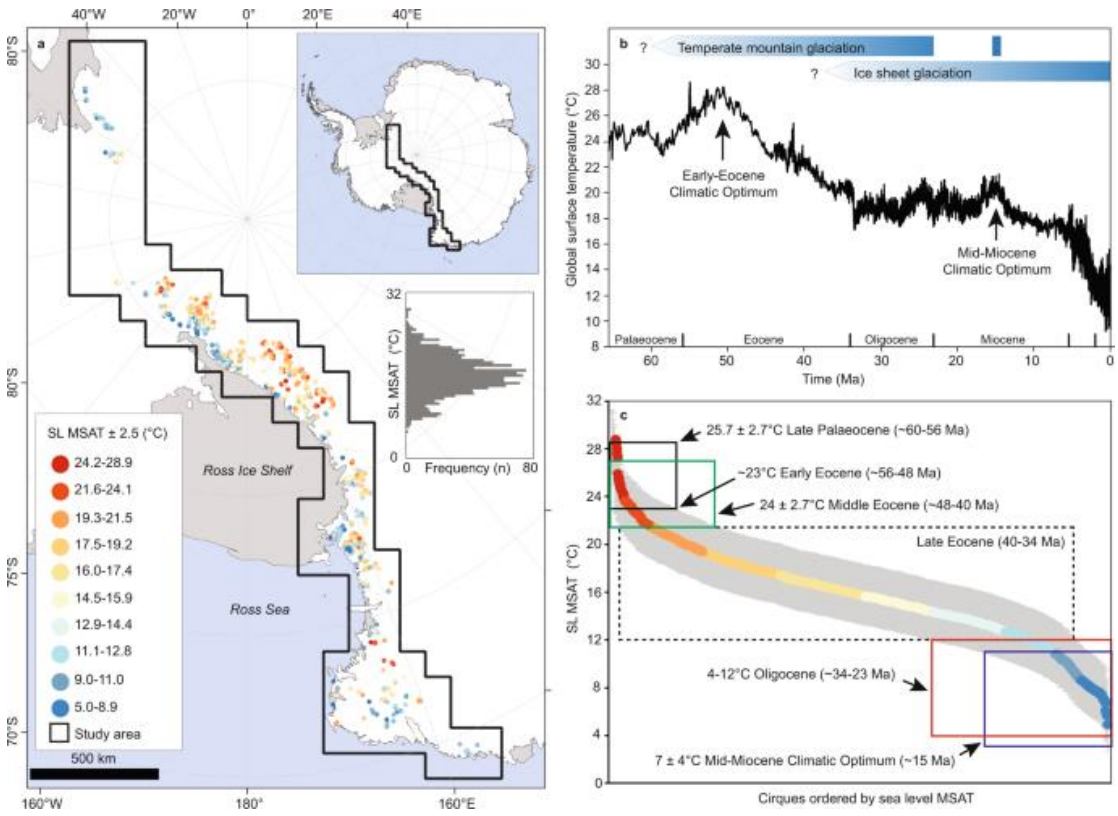

Figure 1. A Glacier-free cirques (n = 1292) in the Transantarctic Mountains coloured according to the sea level mean summer air temperature (SL MSAT) required for them to be occupied by temperate (warm-based) mountain glaciers. The inset histogram shows the frequency distribution of SL MSAT. b Global surface temperature data for the Cenozoic4, highlighting key climatic periods referred to in the text, and our interpretation of the glacial history of the TAM. c Cirques ordered by SL MSAT (grey area represents the ±2.5 °C MSAT uncertainty) required for them to be occupied by temperate mountain glaciers. Colours are based on the values in subplot (a). Antarctic temperature estimates for different time periods in subplot (c) are based on published data from biological proxies.

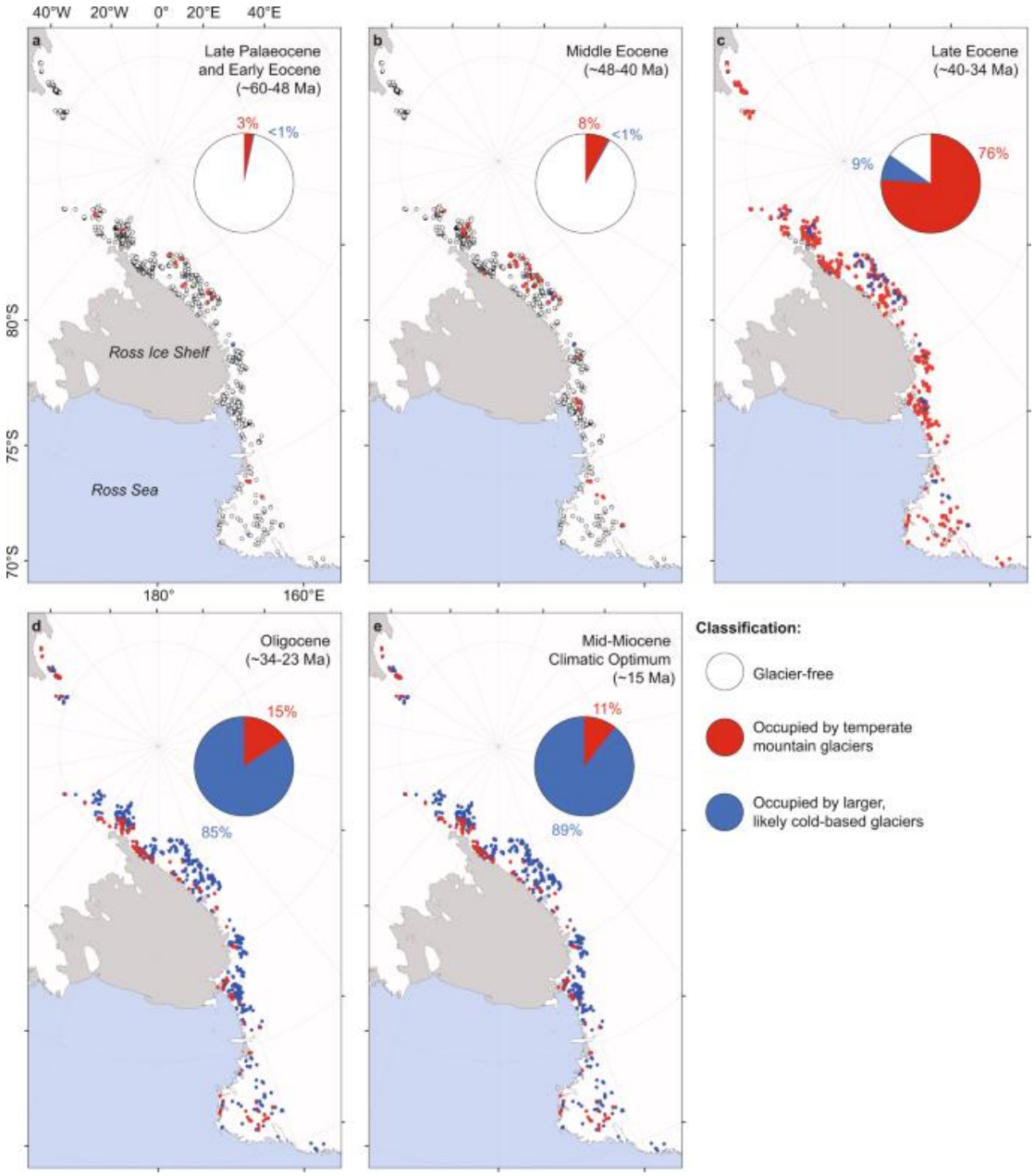

Figure 2. a-e Pie charts show the percentage of cirques classified as glacier free (white), occupied by temperate mountain glaciers (red %), and occupied by larger, likely cold-based glaciers (blue %) for the total population (n = 1292). Antarctic coastline data from the SCAR Antarctic Digital Database.

5. 中亚东部黄土-古土壤沉积的分选系数揭示末次冰期西伯利亚高压的强度变化

翻译人：张靖宇 zhangjy6@sustech.edu.cn

Cheng L, Song Y, Yang L, et al. ***Variations of the Intensity of the Siberian High During the Last Glacial Revealed by the Sorting Coefficient of Loess-Paleosol Deposits in Eastern Central Asia*** *[J]. Paleoceanography and Paleoclimatology, 2022: e2022PA004468.*

https://doi.org/10.1029/2022PA004468

摘要：中亚东部具有干旱环境，经常发生沙尘暴。现代观测表明，中亚东部的沙尘暴频率主要受西伯利亚高压（SH）强度的调控。然而，对影响 SH 变化的过程缺乏了解，限制了我们理解沙尘暴的成因及其预测。在这项研究中，我们进行了中亚东部一个黄土剖面的重矿物组合和沉积物粒度的测试，这些数据跨越了末次冰期。结合以前发表的结果，我们提出，黄土-古土壤序列中的分选系数是指示风强度中比常用的平均粒径和粒径组分更非常敏感的指标，因此也代表了 SH 的强度，也受风尘来源和植被变化的影响。我们的分选系数序列清楚地揭示了 Heinrich 事件，以及显著的~5 kyr Bond 旋回。较大的分选系数对应更多的三宝洞石笋 $\delta^{18}O$ 值的消耗，揭示了末次冰期，SH 和东亚夏季风强度之间的反相关系。分选系数序列也支持北极冰盖对 SH 强度的重大影响。

ABSTRACT: Eastern Central Asia has an arid environment and experiences frequent dust storms. Modern observations indicate that the dust storm frequency in eastern Central Asia is modulated mainly by the intensity of the Siberian High (SH). However, a lack of knowledge about the process influencing the variation of the SH limits our ability to understand the genesis of dust storms and their predictions. In this study, we present data on heavy mineral assemblages and sediment grain size in a loess section in eastern Central Asia, spanning the last glacial. Combined with previously published results, we propose that the sorting coefficient in loess-paleosol sequences is a more sensitive proxy for wind intensity—and thus for the intensity of the SH—than the commonly used proxies of the mean grain size and grain size fractions, which are also influenced by changes in dust source and vegetation cover. Our sorting coefficient series clearly reveals Heinrich events, as well as the prominent ~5 kyr Bond cycle. Larger sorting coefficients correspond to more depleted Sanbao

Cave stalagmite δ18O values, revealing an antiphase relationship between the intensity of the SH and the East Asian Summer Monsoon during the last glacial. The sorting coefficient series also support the significant influence of Arctic sea-ice cover on the intensity of the SH.

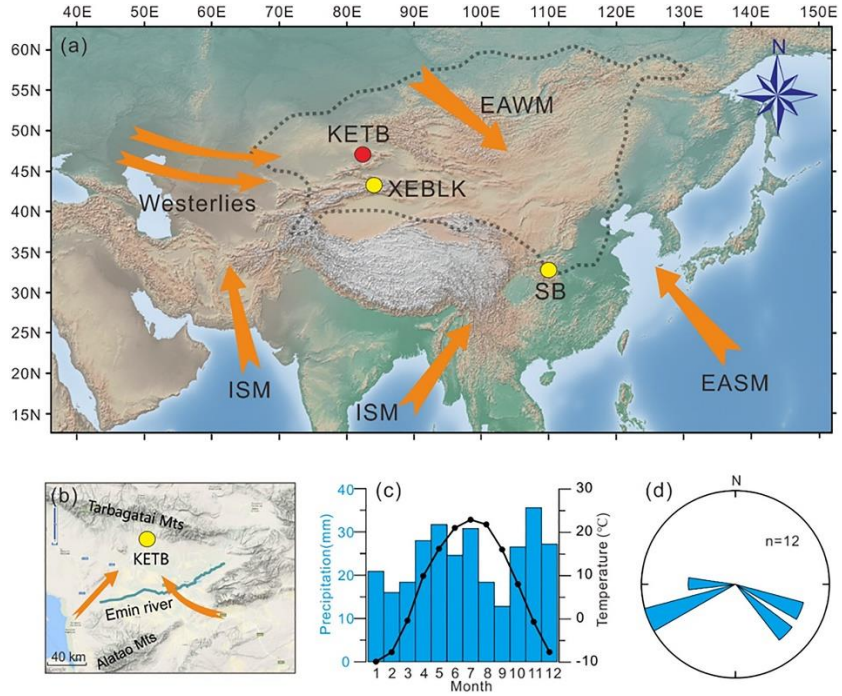

Figure 1. (a) The study area and major modern atmospheric circulation patterns. The closed dotted line indicates the modern range of the Siberian High after Zhang et al. (2015); XEBLK = Xiaoerbulake (Cheng, Song, Chang, et al., 2020); KETB = Kurtobe (this study); SB = Sanbao (Cheng et al., 2016); ISM = Indian Summer Monsoon; EASM = East Asian Summer Monsoon; EAWM = East Asian Winter Monsoon; (b) Topographic map of the Tacheng Basin with the near-surface winds directions. (c) Mean monthly precipitation and temperature for 1981–2010 (data from the China Meteorological Data Network: http://data.cma.cn/); (d) Rose diagram of the monthly gale direction recorded by the Tacheng observation station in 2013.

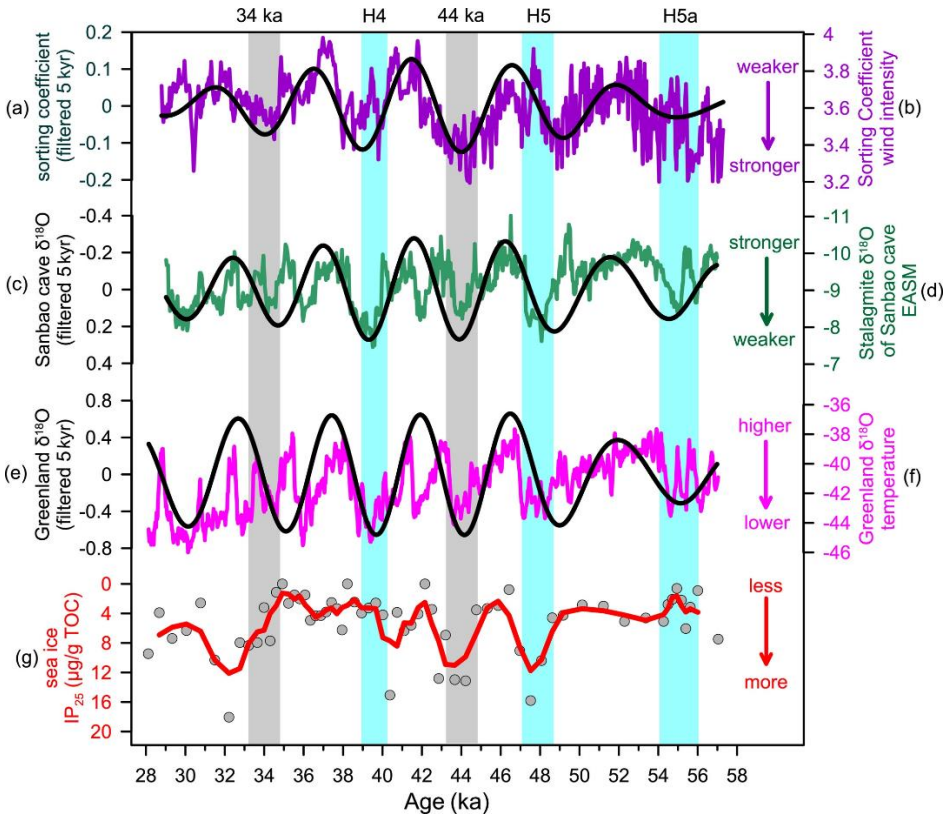

Figure 2. (a) Bandpass-filtered 5 kyr component of the sorting coefficient of the Kurtobe (KETB) loess, (b) sorting coefficient of the KETB loess, (c) bandpass-filtered 5 kyr component of the Sanbao Cave stalagmite δ18O record, (d) Sanbao Cave stalagmite δ18O record (Cheng et al., 2016), (e) bandpass-filtered 5 kyr component of the Greenland ice core δ18O record, (f) Greenland ice core δ18O record (Rasmussen et al., 2006) and (g) record of sea ice cover (gray dots) from the southeastern Norwegian Sea (Hoff et al., 2016), smoothed with a three-point running average (red curve). The cyan bars indicate Heinrich events, and the gray bars indicates the cold stages at ~44 and ~34 ka.

6. 量化碎屑锆石记录与构造背景之间的联系

翻译人：刘伟 inewway@163.com

Jian D, Williams S E, Yu S, et al. ***Quantifying the Link Between the Detrital Zircon Record and Tectonic Settings*** *[J]. JGR solid Earth, 2022: e2022JB024606.*

https://doi.org/10.1029/2022JB024606

摘要：板块构造重建描述了大陆运动的历史以及板块边界如何演化。传统上，板块构造重建依赖海洋地球物理资料和古地磁数据作为主要的定量约束。然而，这些数据并不能约束俯冲带和板块边界的运动路径。因此重建过去板块构造的完整结构必须依靠其他方法。在这里，我们使用了比先前锆石数据更大的数据集，研究了碎屑锆石年龄谱在描述深部构造背景方面的适用性。根据接近沉积年龄的锆石年龄比例，我们分析了重建的板块边界和不同构造背景分类下样本点之间的亲缘性，发现这一方法在划分汇聚板块构造背景方面有高达 70%的成功率。结果不受诸如每个碎屑样品中可用的锆石颗粒数量或样品沉积年龄的不确定性等因素的影响。这一方法在划分伸展环境(如裂谷盆地)的能力还不太清楚。然而，泛大陆尺度上更广泛的结果表明，构造分类的锆石样品形成了一个一致的模式：以年轻锆石为主的样品位于超大陆外围，而泛大陆核心的样品则以比沉积年龄更老的颗粒为主。这一结果表明，锆石数据可以帮助量化板块重建的不确定性，并能区分元古代超大陆可能的模型。

ABSTRACT: Full-plate reconstructions describe the history of past continental motions and how plate boundaries have evolved to accommodate these motions. Traditionally, tectonic reconstructions relied on geophysical data from the oceans and paleomagnetism as the primary quantitative constraints. However, these data do not directly constrain the paths of subduction zones or other plate boundaries, so reconstructing the complete configurations of tectonic plates in the past must rely on alternative methods. Here, we investigate the applicability of detrital zircon age spectra to characterize tectonic settings in deep time using a much larger data set than previously considered. We analyzed the proximity between reconstructed plate boundaries and sample sites assigned to different tectonic categorizations based on the proportion of zircon ages close to the depositional age and found that the categorization has an ~70% success rate in distinguishing convergent settings.

Results are not strongly influenced by factors such as the number of zircon grains available within each detrital sample or uncertainty in the depositional age of the sample. The ability of the categorization to define extensional settings, such as rift basins, is less clear. Nonetheless, the broader pattern of results at the scale of Pangea shows that categorized zircon samples form a coherent pattern, where samples with dominantly young zircons lie at the supercontinent periphery while samples in the core of Pangea are dominated by grains much older than the age of deposition. This result suggests that zircon data could help to quantify uncertainties in full-plate reconstructions and discriminate between competing models for Proterozoic supercontinents.

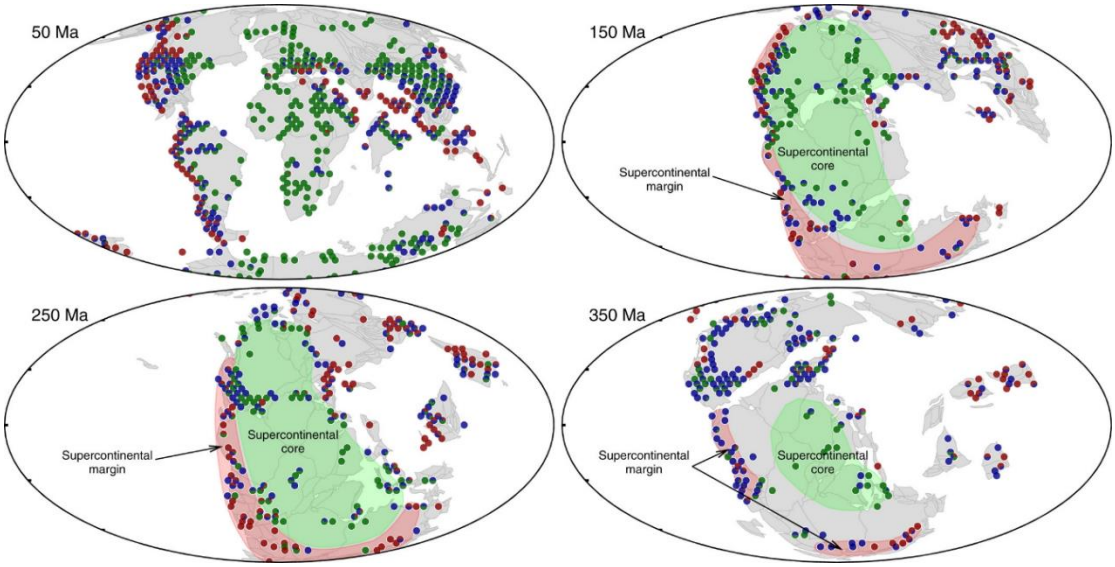

Figure 1. Summary diagram illustrating broad trends in geographic distribution of sample categories across the history of Pangea assembly and dispersal. Reconstructions are shown for 50, 150, 250, and 350 Ma, with each map showing samples with depositional ages within ±50 Ma of the reconstruction age so that all samples from the last 400 Myr appear on one of the panels. The map of 350 Ma is plotted in fixed-South America coordinates. The maps illustrate the dominance of category A samples around the periphery of Pangea while category C samples characterize the supercontinent core.

7. 在小冰河期早期欧洲西风带的分裂

翻译人：杨会会 11849590@mail.sustech.edu.cn

Wang H B, Wang X Y, Perez-Mejias C, et al., ***Split westerlies over Europe in the early Little Ice Age*** *[J]. Nature communications. 2022,13,4898.*

https://doi.org/10.1016/j.quascirev.2022.107581

摘要：小冰河期(LIA；约公元 1450 年至 1850 年)是过去千年来记录最完整的寒冷时期，其特点是火山活动频繁，太阳活动不活跃，北极海冰覆盖高度变化。过去对 LIA 大西洋环流变化的研究参考了北大西洋涛动(NAO)，但最近的研究指出，LIA 的气候模式似乎具有 NAO 模拟所不能捕捉到的复杂性。在这里，我们提出了一个来自意大利北部，对降水敏感的石笋记录，这个新的记录覆盖了过去 800 年。我们的研究表明，在小冰期早期(1470-1610 年)，北欧上空大气脊的增加，使西风带远离中欧和北欧，这可能是北极海冰同时减少造成的。随着北半球高纬度地区持续的冰融化和未来几年太阳辐射的下降，早期的 LIA 的状况可能会在未来几十年充当欧洲水文气候条件的相似型。

ABSTRACT: The Little Ice Age (LIA; ca. 1450–1850 C.E.) is the best documented cold period of the past millennium, characterized by high-frequency volcanism, low solar activity, and high variability of Arctic sea-ice cover. Past studies of LIA Atlantic circulation changes have referenced the North Atlantic Oscillation (NAO), but recent studies have noted that LIA climate patterns appear to possess complexity not captured by an NAO analogue. Here, we present a new precipitation-sensitive stalagmite record from northern Italy that covers the past 800 years. We show that in the early LIA (1470-1610 C.E.), increased atmospheric ridging over northern Europe split the climatological westerlies away from central and northern Europe, possibly caused by concurrent Artic sea-ice reduction. With ongoing ice melting in the northern high latitudes and decreasing solar irradiance in the coming years, the early LIA may potentially serve as an analogue for European hydroclimatic conditions in the coming decades.

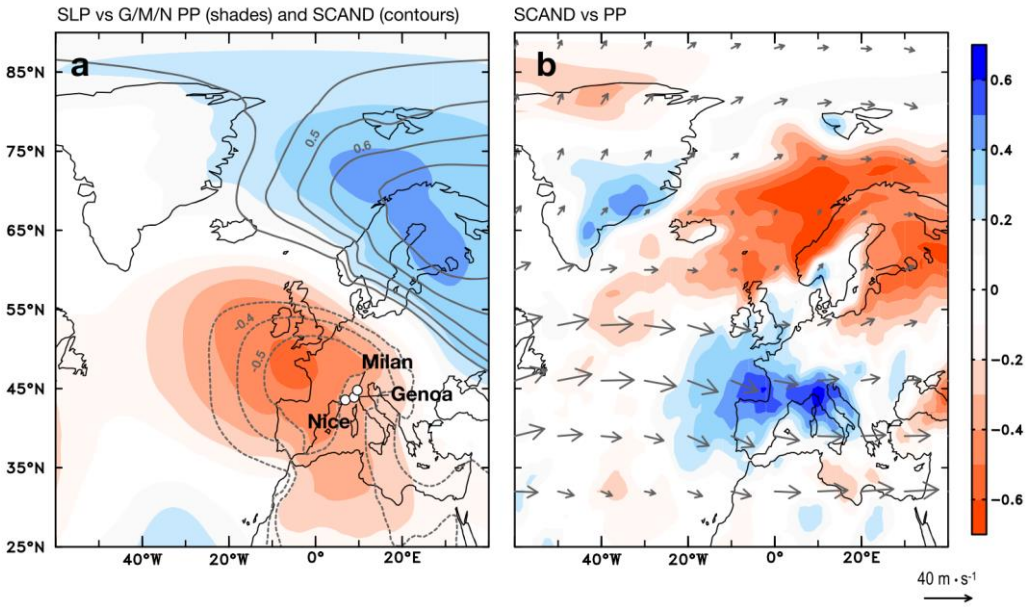

Figure 1. Climate and Atlantic sea-level pressure (SLP) variability. a Correlation between SLP and (i) average precipitation at Genoa, Milan and Nice stations (G/M/N PP) (shades); (ii) Climate Prediction Center (CPC) Scandinavia index (SCAND) (contours) during September-February in 1950-2008 C.E. b Vectors: climatological winds at 200-mb level plus regression of 200-mb winds on SCAND index multiplied by two standard deviations of SCAND index during September-February in 1950-2008 C.E., indicating a positive SCAND condition. Shades: correlation between SCAND and ground precipitation during September-February in 1950-2008 C.E. The shades and contours indicate the correlation coefficient(s) above 90% confident level. Climate data are from 20th century reanalysis v3.

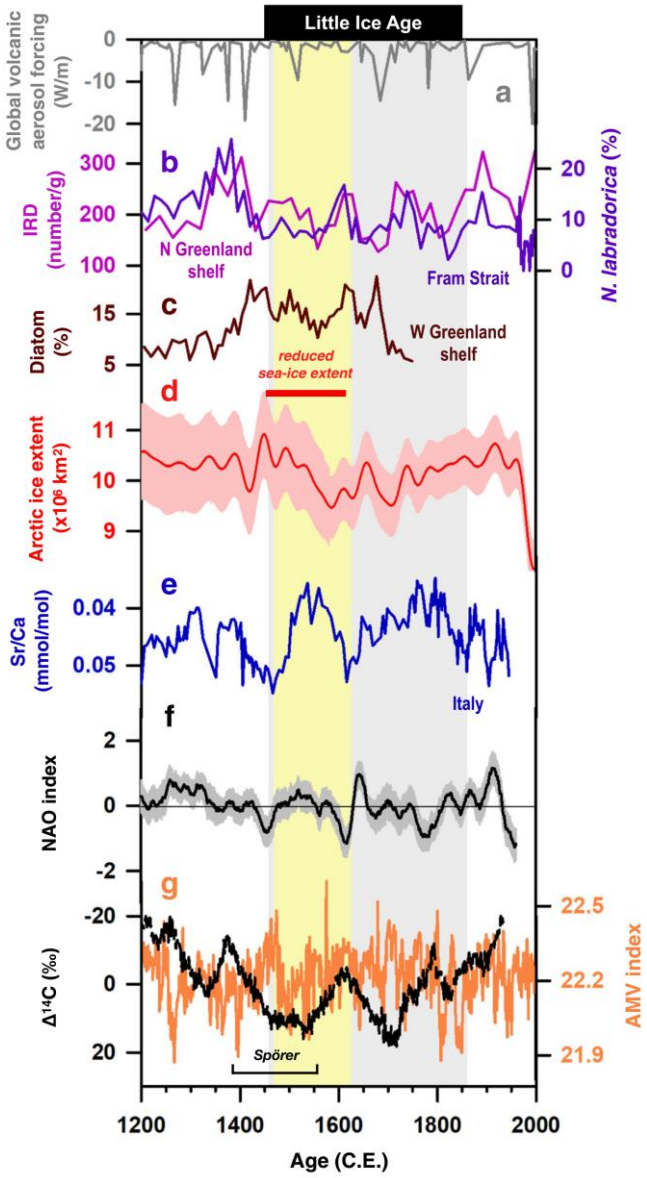

Figure 2. Comparison of volcanic forcing, solar activity, sea-ice variability, and Bàsura record. a Global volcanic aerosol forcing. b Violet: concentration of benthic foraminifera from the North Greenland shelf (PS2641-4; Supplementary Fig. 2) as an indicator of sea-ice cover. Pink: ice-rafted debris (IRD) (MSM5/5; Supplementary Fig. 2) from the Fram Strait. High values of these two records denote large sea-ice cover. c Five-point averaged diatom concentration (Thalassiosira nordenskioeldii) from the west Greenland shelf (GA306-4; Supplementary Fig. 2). High value denotes large sea-ice cover. d Red: 40-year smoothed reconstructed late summer Arctic sea-ice extent. e Bàsura Sr/Ca record. f Reconstructed NAO index. g Orange: Atlantic Multidecadal Variability index. Black: total solar irradiance. The intervals of the Spörer Minimum (1388-1558 C.E.)12 and decreased sea-ice event (1450-1620 C.E.) are marked. The grey vertical bar denotes the Little Ice Age. The yellow vertical bar highlights the period 1470-1610 C.E.

8. 关于考古植物遗迹中致密结构的一些记录：X 射线荧光计算机断层扫描的应用

翻译人：曹伟 11930854@qq.com

Calo, C M, Rizzutto, M A, Pérez, C A, et al. ***Some Notes on Dense Structures Present in Archaeological Plant Remains: X-ray Fluorescence Computed Tomography Applications****[J]. Minerals 2022, 12, 1130.*

https://doi.org/10.3390/min12091130

摘要：本研究描述了蒙特卡洛 (6000-700 cal. AP-SW Amazonia) 未烧焦的植物遗迹中存在的致密体或结构的组成和来源。该研究旨在从软组织矿化过程的角度揭示该植物遗骸与遗址沉积基质在 200 多年(至少)以来的相互作用。用 XFCT、x 射线显微 ct 和 SEM-EDS 技术检查了两个样品，以揭示 Ca、K、Mn、Fe、Ti、Si、S、Cu、Br、Rb、Sr、Zn 和 Zr 的存在和分布。这些属性与沉积基底的 ED-XRF 和 XRD 测量数据相结合。结果表明，在植物体和解剖结构中存在的化学元素，有的与沉积环境有关，有的与内生环境有关。它们主要包括 Rb 和 Br，被解释为内部组织降解过程的结果，主要存在于内部组织。除 Sr 和 Zr 外，其余元素均有一部分从沉积基质进入并分散到样品结构中。它的存在可归因于通过最外层组织的附着、扩散和浸渍等机制，在那里它们大多集中。大部分致密体的成分由内源元素和外源元素组成。

ABSTRACT: This study describes the composition and provenance of dense bodies or structures present in uncharred plant vestiges recovered at Monte Castelo (6000-700 cal. AP-SW Amazonia). It aimed to disclose some aspects of this plant remains interactions with the sedimentary matrix of the site over the 200 years (at least) since its initial deposit, from the point of view of the soft tissue mineralization processes. Two specimens were examined using XFCT, X-ray MicroCT, and SEM-EDS techniques to reveal the presence and distribution of Ca, K, Mn, Fe, Ti, Si, S, Cu, Br, Rb, Sr, Zn, and Zr. These attributes were integrated with compositional ED-XRF and XRD measured data from the sedimentary substrate. Results show that some of the chemical elements present in solid bodies and anatomical structures of the plant remains refer to the sedimentary environment, while others have an endogenous origin. These include mainly Rb and Br, which were interpreted as the

result of degradation processes of the internal tissues, where they are mainly present. Except Sr and Zr, a portion of all the other elements entered and disperse into the sample structures from the sedimentary substrate. Its presence is attributable to mechanisms such as attachment, diffusion and impregnation through the outermost tissues, where they are mostly concentrated. The composition of most of the dense bodies consists of both endogenous and exogenous elements.

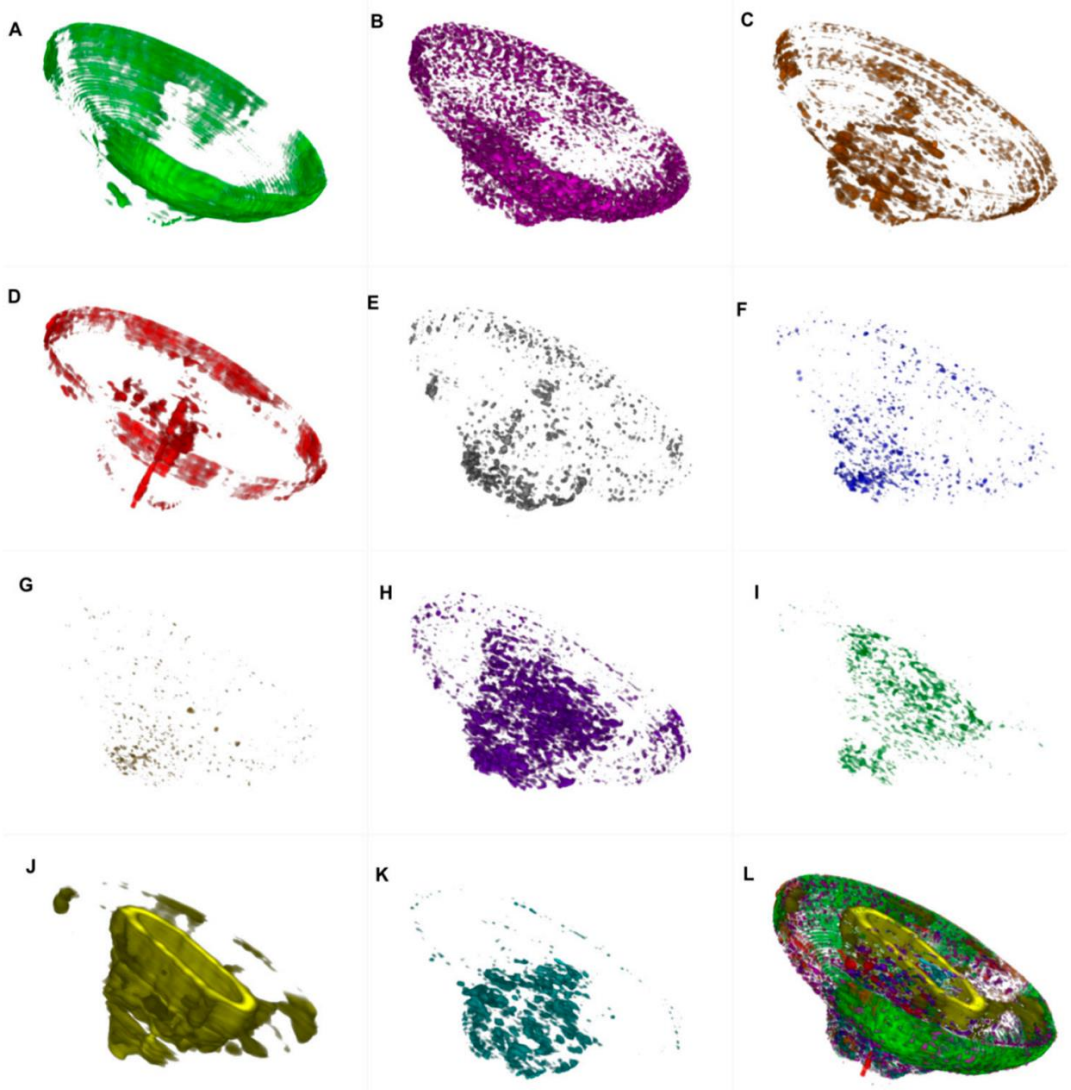

Figure 1. Three-dimensional elemental distribution: (A) Calcium; (B) Potassium; (C) Manganese; (D) Iron; (E) Titanium; (F) Silicon; (G) Sulphur; (H) Copper; (I) Bromine; (J) Rubidium; (K) Zinc; (L) Assembled component 3D distribution. (Software: FIJI-ImageJ 3D Viewer).

9. 印度尼西亚 Karimata 海峡洪水历史对深海氧同位素第 3 阶段和第 5 阶段海平面的制约

翻译人：王浩森 11930841@mail.sustech.edu.cn

Weiss T L, Linsley B K, Gordon A L, et al. ***Constraints on Marine Isotope Stage 3 and 5 Sea Level from the Flooding History of the Karimata Strait in Indonesia****[J]. Paleoceanography and Paleoclimatology, 2022: e2021PA004361.*

https://doi.org/10.1029/2021PA004361

摘要：深海氧同位素 3 阶段间冰期中期（MIS 3）（60–26 ka）的全球平均海平面（GMSL）已证明难以限制。基于冰缘、建模和古海岸线重建的古海平面估算表明，MIS 3 GMSL 显著高于根据深海底栖有孔虫氧同位素（$\delta^{18}O$）和珊瑚记录重建的海平面，这意味着 MIS 3 期间的冰盖要小得多，我们使用西太平洋边缘苏禄海表层和温跃层有孔虫的 $\delta^{18}O$ 和 Mg/Ca，估算了过去 140ka 以来中国南海表层流流入苏禄海的相对变化。结果表明，南海通流部分受 GMSL 变化的控制，GMSL 调整了南海南端 36 米深的卡里马塔海峡的深度。我们将 MIS 3 开始和结束时的最大允许 GMSL 分别限制为：−22±6 m 和−29±5 m， 间冰期 MIS 5c 和 5a（117-72 ka）期间的最小允许 GMSL 范围分别为−3±8 至−8±8 m 以及−11±7 和 12±7m。我们的结果限制了 MIS 3 GMSL，但不排除更高的 MIS 3 冰缘、建模和基于古海岸线的 MIS 3GMSL 估计或更低的基于珊瑚和海水 $\delta^{18}O$ 的估计。我们的结果支持最高的 MIS 5a 和 5c GMSL 估计值，并确认当人类首次抵达婆罗洲时，巽他大陆架在 MIS 3 期间充当了人类和大型动物迁徙的陆桥。

ABSTRACT: Global mean sea level (GMSL) during intermediate interglacial Marine Isotope Stage 3 (MIS 3) (60–26 ka) has proven difficult to constrain. Paleo-sea level estimates based on ice margin, modeling, and paleo-shoreline reconstructions indicate that MIS 3 GMSL was substantially higher than reconstructed from deep-ocean benthic foraminifera oxygen isotope ($\delta^{18}O$) and coral records, implying much smaller ice sheets during MIS 3. Here, we use the $\delta^{18}O$ and Mg/Ca chemistry of surface and thermocline dwelling foraminifera in the Sulu Sea in the western Pacific margin to estimate relative changes of the influx of South China Sea surface flow through the Sulu Sea over the last 140 ka. We show that this South China Sea throughflow is controlled in part by changes in

GMSL modulating the depth of the 36 m deep Karimata Strait at the southern end of the South China Sea. We constrain maximum allowable GMSL at the beginning and end of MIS 3 to −22 ± 6 and −29 ± 5 m, respectively, and minimum allowable GMSL during interglacial stages MIS 5c and 5a (117–72 ka) to range from −3 ± 8 to −8 ± 8 m and −11 ± 7 to −12 ± 7 m, respectively. Our results constrain MIS 3 GMSL, but do not rule out higher MIS 3 ice margin, modeling, and paleo-shoreline-based MIS 3 GMSL estimates or lower coral and seawater $\delta^{18}O$-based estimates. Our results favor the highest MIS 5a and 5c GMSL estimates and confirm that the Sunda Shelf served as a land-bridge for human and megafauna migration during MIS 3 when humans first arrived in Borneo.

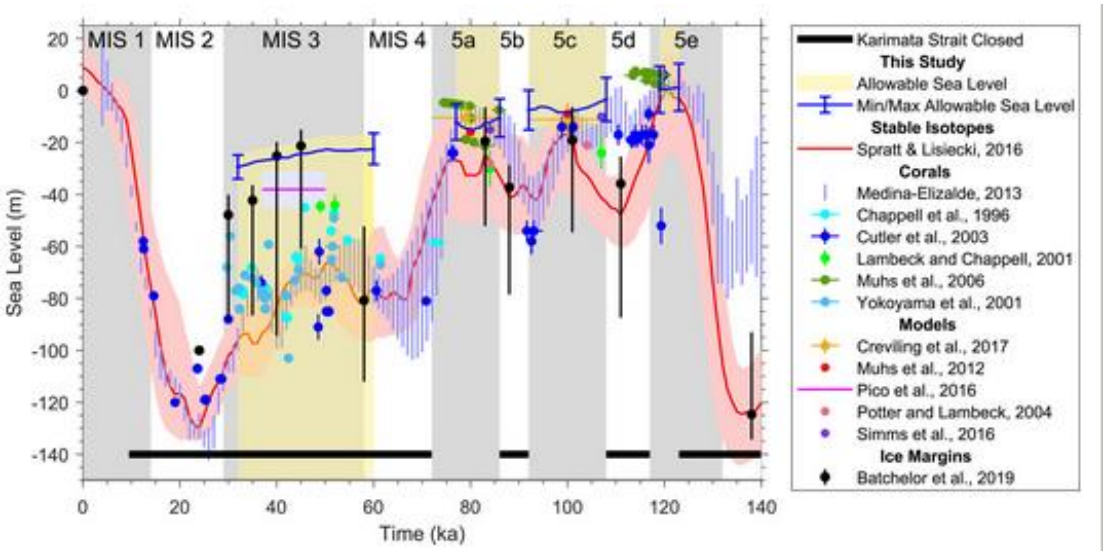

Figure 1. Our estimates of maximum allowable sea level during Marine Isotope Stage 3 (MIS 3) and minimum allowable sea level during MIS 5 compared to other sea level constraints. Blue bars for our study represent the Glacial Isostatic Adjustment (GIA) corrected effective depth of the Karimata Strait adjusted for the average subsidence rate. Uncertainty bars represent the GIA corrected (Creveling et al., 2017) effective depth of the Karimata Strait adjusted for the maximum and minimum subsidence (Sarr et al., 2019) rate along with a ±3 m uncertainty to account for sedimentation. Our sea level constraints view any sea level within the yellow shading as equally likely because our constraints only stipulate sea level must have been below the effective depth of the Karimata Strait during MIS 3 and above the depth of the strait during MIS 5a, 5c, and 5e. Thick black bars near the bottom of the plot represent periods when we argue the Karimata Strait was closed. Evidence for a closed Karimata Strait during MIS 3, MIS 5b, 5d, and early 5e and before come from this study. It is possible the Karimata Strait was also closed during late MIS 5a and early and late MIS5 5c, but the evidence in our reconstruction is unclear. Evidence for a closed Karimata Strait during early MIS 1 and MIS 2 comes from Linsley et al. (2010) and Rosenthal et al. (2003a). A closed Karimata Strait during MIS 4 can be inferred from any of the other sea level records covering that interval shown in this figure.

10. 从中国黄土沉积物中获得的过去三个冰期-间冰期旋回气候变化的绝对年代记录

翻译人：王敦繁 Dunfan-w@foxmail.com

Zhang, J., Hao, Q., and Li, S.-H., 2022, ***An absolutely dated record of climate change over the last three glacial–interglacial cycles from Chinese loess deposits****[J], Geology, 50, 2022, 1116–1120, https://doi.org/10.1130/G50125.1*

摘要：长期以来，中国黄土-古土壤序列记录了第四纪冰川-间冰期旋回，被认为是除深海沉积物之外古气候记录的良好载体。然而，中国黄土高原距今约 130 ka 以上的黄土-古土壤序列的绝对年代学研究还很少。我们首次对中国黄土高原中部经典的洛川黄土剖面进行了 350 ka 的高分辨率的释光测年。利用培根年龄深度模型对释光年龄进行建模，得到了释光年龄框架。结果表明，在轨道时间尺度上，洛川黄土的积累在近 3 个冰期-间冰期旋回中是连续的。新的年龄框架解决了几个边界上轨道校正年龄模型之间的差异，并提供了新的证据，支持将海洋同位素阶段 8/9 边界年龄从 300 ka 重新分配到约 280 ka。我们的结果还表明，已发现的中国黄土高原黄土沉积的天文时间尺度在过去的~ 2.6 百万年之间是可靠的，这些发丝现也支持其相关区域和全球气候的解读。

ABSTRACT: Chinese loess-paleosol sequences have long been regarded as the continental counterpart of deep-sea sediments in terms of their record of the Quaternary glacial–interglacial cycles. However, absolute chronologies for loess-paleosol sequences older than ca. 130 ka on the Chinese Loess Plateau are scarce. We conducted the first high-resolution luminescence dating, extending back to 350 ka, of the classical Luochuan loess section of the central Chinese Loess Plateau. Bacon age-depth modeling of the luminescence ages was used to obtain an age framework. The results indicate that on orbital timescales, loess accumulation at Luochuan was continuous over the last three glacial–interglacial cycles. The new age framework resolves discrepancies between orbitally tuned age models at several boundaries and provides new evidence supporting the reassignment of the Marine Isotope Stage 8/9 boundary age from 300 ka to ca. 280 ka. Our results also suggest that published astronomical timescales for the loess deposits of the Chinese Loess

Plateau over the last ~2.6 m.y. are probably broadly reliable, as are the related regional and global climatic interpretations.

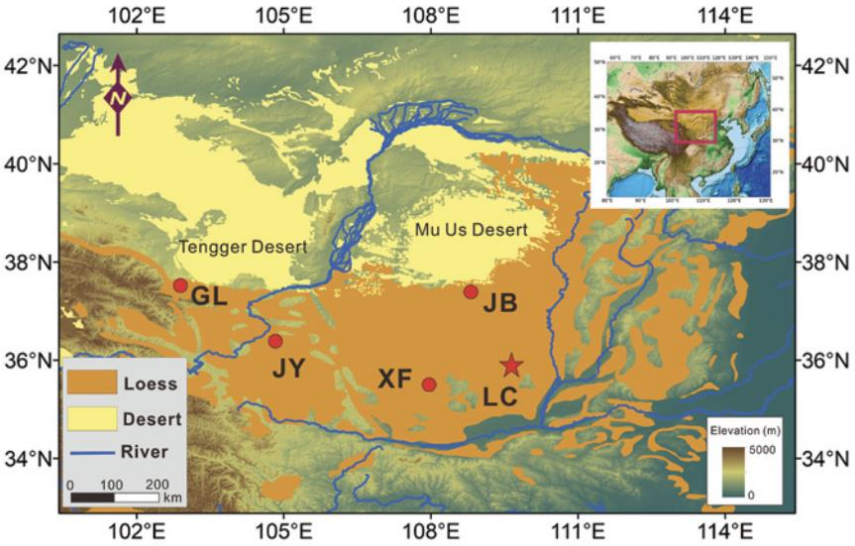

Figure 1. Map of the Chinese Loess Plateau (CLP) and locations of the Luochuan section and other sections mentioned in the text. LC—Luochuan, JB— Jingbian, XF—Xifeng, JY—Jingyuan, GL—Gulang. Map is modified from Wu et al. (2019). Base map is a digital elevation map from the database of Shuttle Radar Topogra- phy Mission (SRTM) 90 m Digital Elevation Data (https://srtm.csi.cgiar.org /srtmdata/).

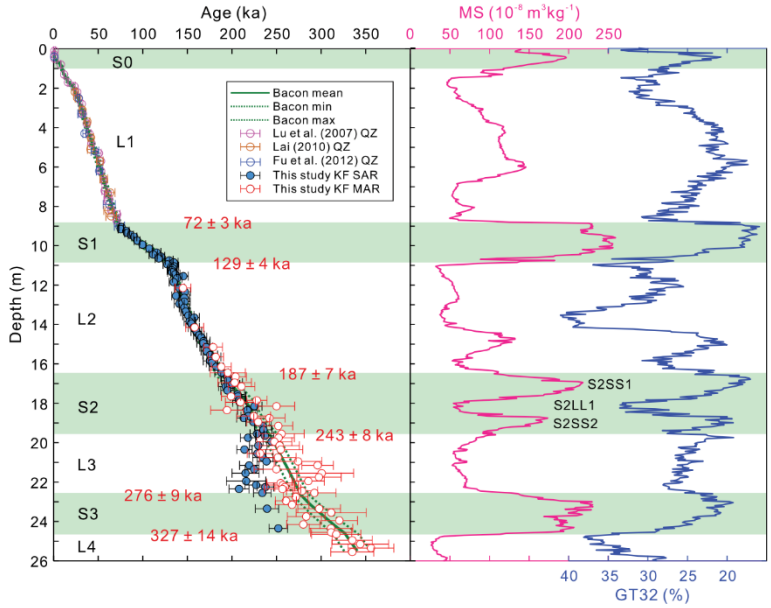

Figure 2. Bacon age-depth model for the Luochuan section of the Chinese Loess Plateau. Ages of the boundaries modeled using the Bacon age-depth method are labeled. Note that the single-aliquot regenerative-dose (SAR) ages above the L2/S2 boundary and the multiple-aliquot regenerative-dose (MAR) ages below the L2/S2 boundary were used for Bacon modeling. The magnetic susceptibility (MS) and grain size GT32 (>32 μm fraction) data are from Hao et al. (2012). KF—K-feldspar; QZ—quartz.

11. 模拟岩墙在垂直和水平方向上的生长

翻译人：张伟杰 12031188@mail.sustech.edu.cn

Pansino S, Emadzadeh A, Taisne B. ***Modeling dike propagation in both vertical length and horizontal breadth****[J]. Journal of Geophysical Research: Solid Earth, e2022JB024593.*

https://doi.org/ 10.1029/2022JB024593

摘要：我们展示了岩墙生长的模拟实验，随后建立了一个部分是解析的部分是基于经验观察的水平和垂直生长的数值模型。实验结果表明，在浮力变得显著之前，生长率是相似的，之后，垂直增长占主导地位。对均匀介质数值模型设定不同的条件：（1）恒定通量，裂缝限制生长；（2）恒定通量，粘性限制；（3）取决于驱动压力和岩墙尺寸的可变通量。这些条件区分了两种情况，一种是岩浆流入依赖于较深层的岩浆来源（例如，独立于岩脉几何形状的岩浆通道），另一种是岩浆流入依赖于岩墙，岩浆流入量可以随着增长而变化。在所有情况下，垂直生长与水平生长的比率跟浮力与岩浆源压力的比值成正比，其中浮力驱动垂直生长。我们对在 Piton de la Fournaise 观察到的岩墙建立的数值模型进行测试，该模型中尺寸是使用大地测量和地震数据估计的。结果表明，使用 50 - 300 kg/m3 的岩浆-地壳密度差、30 - 300 Pa • s 的粘度、50 - 750 m3/s 的流入量和 ~10 GPa 的剪切模量，可以再现其最终尺寸。模拟的岩浆和围岩岩石参数与以往的火山研究一致，但其通量高于通常在喷发期间观察到的通量。这意味着一个可变的注入条件，其中通量在岩墙生长过程中达到峰值，在喷发开始时下降。

ABSTRACT: We present analogue experiments on dike propagation, followed by a numerical model of horizontal and vertical growth, which is partially analytical and partially based on empirical observations. Experimental results show that the growth rates are similar until buoyancy becomes significant and, afterwards, vertical growth dominates. The numerical model is defined for different conditions in a homogeneous medium: (1) constant flux, fracture-limited propagation; (2) constant flux, viscous-limited propagation; (3) variable flux dependent on the driving pressure and dike dimensions. These conditions distinguish between cases when the influx depends on the deeper

source of magma (e.g., a conduit, independent of the dike geometry) and when it depends on the dike, so the influx can change as it grows. In all cases, the ratio of vertical to horizontal propagation is proportional to the ratio of buoyancy pressure to source pressure, in which buoyancy drives vertical propagation. We test the numerical model on dikes observed at Piton de la Fournaise, in which the dimensions were estimated using geodetic and seismic data. The results show that the final dimensions can be reproduced using magma-crust density differences of 50 to 300 kg/m3, viscosities of 30 to 300 Pa·s, influxes of 50 to 750 m3/s and shear moduli of ~10 GPa. The modeled magma and host rock parameters agree with previous studies of the volcano, while the flux is higher than what is typically observed during eruption. This implies a variable injection condition, in which the flux peaks during propagation and diminishes by the onset of eruption.

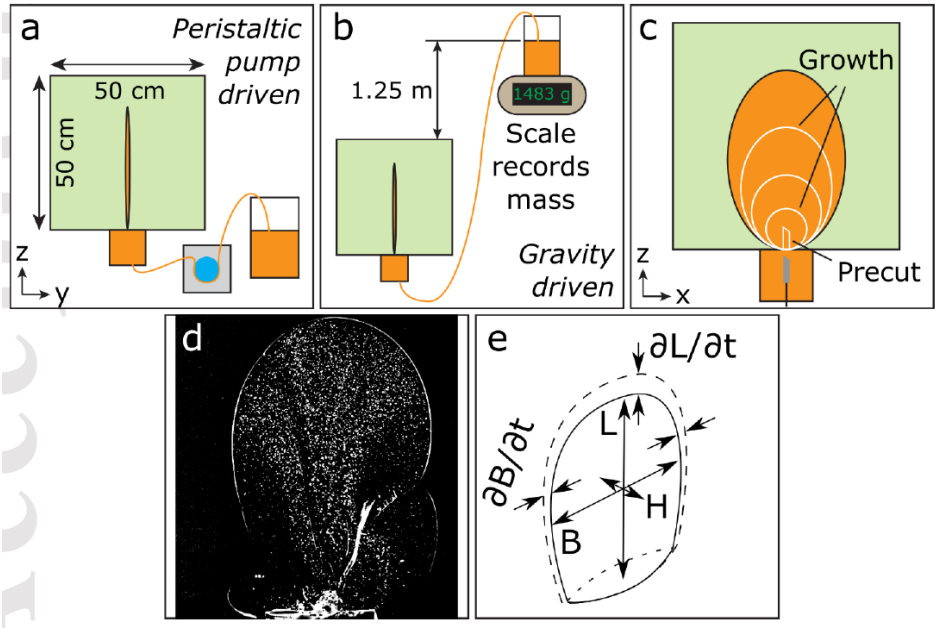

Figure 1. The experimental setup, housed in a 50x50x50 cm3 tank. The magma analogue (here shown in orange) is injected into solid gelatin via (a) a peristaltic pump at a constant influx or (b) gravitation pressure head at a constant pressure. We used a scale to record a time series of mass of the liquid in the supply beaker and estimate the volumetric flux. (c) We made an initial precut into the gelatin to control the orientation of the dike. The dike's growth, which we tracked with a video camera, is generally radial at first and then becomes more vertical when buoyant. (d) An image from experiment 2, which has a small en-echelon dike to the right. Image processing subtracts the background to make the dike stand out. Note particles embedded in the liquid are used for velocimetry, not discussed in this study. The edges of the dike are apparent and can be automatically tracked to record dimensions. (e) Definitions of dike dimensions and growth rates. The $\partial B/\partial t$ totals the growth on both sides of the dike.

12. 碳酸盐风化、CO_2 的分布以及新近纪 CCD 与 pCO_2 的演化

翻译人：李海 12031330@mail.sustech.edu.cn

Louis A D. ***Carbonate weathering, CO_2 redistribution, and Neogene CCD and pCO_2 evolution*** *[J]. Earth and Planetary Science Letters, 2022.*

https://doi.org/10.1016/j.epsl.2022.117801.

摘要：碳酸盐补偿深度（CCD）、海洋碳酸盐 $\delta^{13}C$、大气 pCO_2 和海水的主要离子组成为新近纪地质碳循环过程的演化提供了约束条件。作者利用简单的模型和 LOSCAR 海洋碳系统模型来评估海洋中碳通量的哪些变化对于解释字中新世早期以来的观测是必要的。计算考虑了中新世早期海水温度和离子组成以及一系列可能的 pCO_2 的估计值。陆架—盆地分区的变化可以解释 CCD 为何加深了约 45%。碳酸盐岩向海洋的通量增加(可能范围为 28±12%)是解释其余现象的必要条件。尽管 pCO_2 从早期中新世的 450-900 ppm 值变化到人类活动前的 280 ppm，但海洋-大气碳储库的总规模仅显示出适度的变化或没有净变化，这意味着风化和/或有机碳埋藏导致很少的二氧化碳净消耗。在新近系，Ca^{++}的减少和深水碳酸盐岩饱和度的增加需要深水 CO3 的大量增加，从而导致 DIC/TALK 的降低，这是 pCO_2 分压下降的主要驱动因素。pCO_2 降低的主要驱动力是 CO_2 从大气到海洋的再分配，而不是从过量的硅酸盐风化或有机碳埋藏中净去除 CO_2。新近纪期间碳循环的构造扰动的主要影响是增强碳酸盐风化，而仅对脱气与硅酸盐风化或干酪根氧化与有机碳埋藏的净平衡产生微弱影响。

ABSTRACT: The carbonate compensation depth (CCD), $\delta^{13}C$ of marine carbonate, atmospheric pCO_2 and major ion composition of seawater provide constraints on how geological carbon cycle processes evolved over the Neogene. I use simple models and the LOSCAR ocean carbon system model to assess what changes in carbon fluxes to the ocean are necessary to explain observations since the early Miocene. The calculations consider estimates of early Miocene seawater temperatures and ion composition and a range of possible pCO_2. Changes in shelf-basin partition could explain up to ≈45% the observed CCD deepening. Increased carbonate flux (likely range 28 ± 12 %) to the oceans is necessary to explain the rest. Despite changes in pCO_2 from early Miocene values of 450 – 900 ppm to a pre-anthropogenic value of 280 ppm, the size of the total ocean-

atmosphere carbon reservoir shows only moderate or no net change, implying that weathering and/or organic carbon burial result in little net CO_2 consumption. Decreasing Ca^{++} and increasing deepwater carbonate saturation over the Neogene require a large increase in deepwater CO_3 and leads to decreasing DIC/TALK which is the main driver for falling pCO_2. The primary driver of pCO_2 reduction is redistribution of CO_2 from the atmosphere to the oceans, not net removal of CO_2 from excess silicate weathering or organic carbon burial. The main impact of tectonic perturbation of the carbon cycle during the Neogene is to enhance carbonate weathering while only weakly affecting the net balance of degassing vs. silicate weathering or kerogen oxidation vs. organic carbon burial.

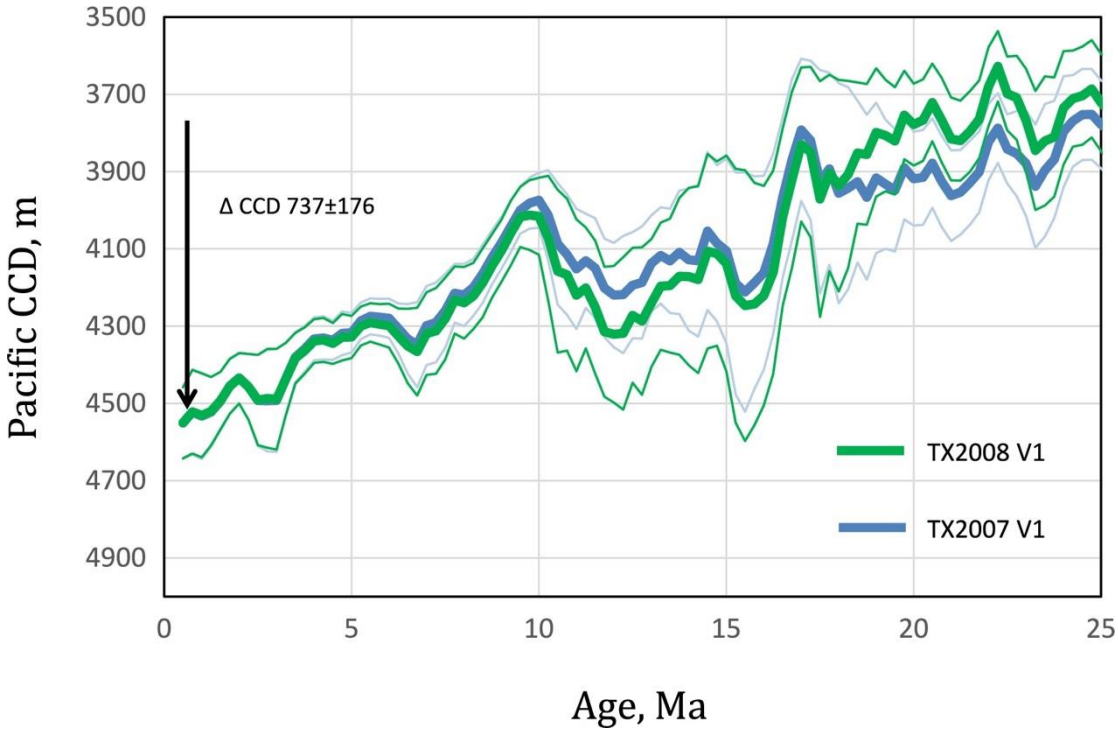

Figure 1. Pacific CCD reconstructed after correction for dynamic topography by Campbell et al., 2018. TX2007 V1 (blue line), TX 2008 V1 (green line). Thin lines are 2 σ uncertainties. Using the reconstruction in Campbell et al. (2018) the mean of the CCD estimates for the 20-21.5 Ma interval is used as a starting condition for the early Miocene and compared to the 0.5 Ma results as an approximation for the modern CCD (the last time slice computed by Campbell et al.). The primary goal is to evaluate the change in the CCD rather than the absolute values. The Pacific CCD deepens from 3813 to 4550 m, for a $\Delta CCD = 737^{+176}/_{-164}$ m using the average of TX2007/08 V1 models.

13. 源区的低铁溶解度限制了南美风尘的铁肥效应

翻译人：张亚南 zhangyn3@mail.sustech.edu.cn

Simonella L E, Cosentino N J, Montes M L, et al. ***Low source-inherited iron solubility limits fertilization potential of South American dust*** *[J] Geochimica et Cosmochimica Acta, 2022, 335, 272-283.*

https://doi.org/10.1016/j.gca.2022.06.032

摘要：在由于低人为排放，大气过程较弱的地方，受到粉尘铁限制的海洋，其铁肥效应很大程度上取决于源区的铁溶解度。南美洲南部（SSA）是一个原始的环境，也是南大洋风尘的主要源区，是对铁肥效应影响最为敏感的地方。因此，现今 SSA 风尘铁肥作用在南大洋的缺乏，被认为反映了源区较低的铁的生物利用率。然而，SSA 风尘地化研究的缺乏阻碍了这一假设的验证。为了解决这个问题，作者对 SSA 粉尘源区进行了首次系统采样。铁淋滤实验表明近源粉尘（全岩）和扬尘（＜63μm）（dust-emitting surface sediments）在纯水（0.05±0.05%）、海水（0.03±0.04%）和 1%硝酸中均为部分溶解，表明与其他地区的粉尘相比，SSA 粉尘的质量归一化铁肥潜力较低。基于粒度、矿物学、元素化学和铁形态测定，作者发现，无论氧化状态如何，高粘土含量、小粒径和顺磁性铁相比非顺磁性铁比例的升高都使得不稳定铁的变化增强。最不稳定的水溶性铁相对粒度的独立变化，及其化学风化指数（CIA）的强负相关可能暗示我们目前低估了比现在更为干燥的冰期，较粗的冰成风尘对生物可利用铁的贡献，该时期大陆化学风化减弱，风尘携带的生物有效铁向南大洋的供应增加。

ABSTRACT: Where atmospheric processing is weak due to low anthropogenic emissions, fertilization of iron-limited oceans by non-volcanic mineral dust aerosols strongly depends on iron solubility at the sources. Southern South America (SSA) is a pristine environment and the main dust supplier to the southern oceans, the most sensitive to iron fertilization. Thus, the present-day lack of SSA dust fertilization of the southern oceans is hypothesized to reflect low source-inherited iron bioavailability. However, a dearth of geochemical studies on SSA dust prevents testing this hypothesis. To remedy this, we conducted the first systematic sampling of SSA dust sources. Iron leaching experiments showed fractional solubilities of close-to-source dust (bulk) and dust-emitting

surface sediments (<63 µm) in pure water (0.05 ± 0.05%), seawater (0.03 ± 0.04%) and 1% nitric acid (5 ± 6%) that imply a low mass-normalized fertilization potential of SSA dust compared to dust from other regions. Based on grain size, size-resolved mineralogy, elemental chemistry and iron speciation determinations, we found that variability in labile iron is enhanced by high clay contents, small grain size and higher proportions of paramagnetic versus non-paramagnetic iron, irrespective of oxidation state. The independence of the most labile, water-soluble iron on grain size and its strong negative correlation to the Chemical Index of Alteration may imply that we currently underestimate the role of coarse glaciogenic dust as a supplier of bioavailable iron during drier-than-present ice ages when continental chemical weathering was reduced, and during which enhanced supply of dust-borne bioavailable iron to the southern oceans is observed.

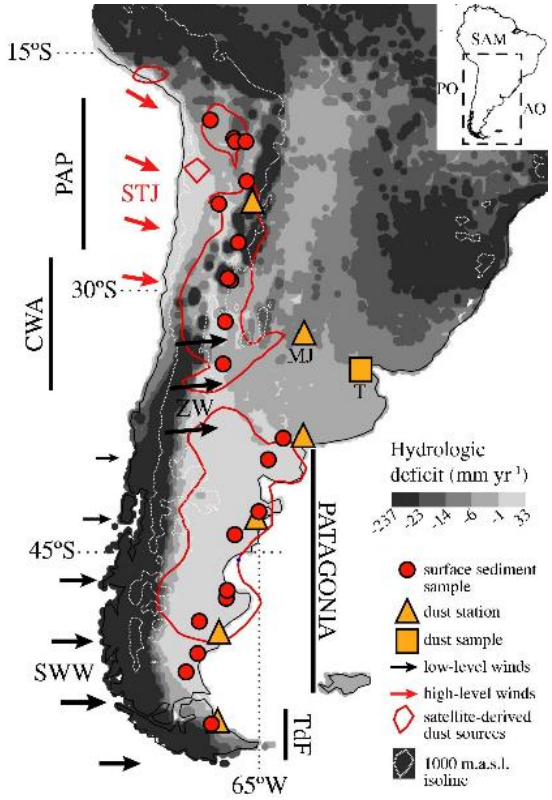

Figure 1. The South American Arid Diagonal. Dust contours indicate areas where the absorbing aerosol index derived from the Total Ozone Mapping Spectrometer was ≥ 0.7 during ≥ 7 days per month, for a 1980 – 1992 climatology (Prospero et al., 2002). Hydrologic deficit is calculated as total evaporation minus total precipitation, which were derived from monthly ERA5-Land reanalysis data between 1981 and 1992. The 1000-meter above sea level (m.a.s.L.) isoline corresponds to the 0.25° lat-lon resolution TerrainBase dataset. TdF: Tierra del Fuego, CWA: Central Western Argentina, PAP: Puna-Altiplano Plateau, MJ: Marcos Juárez, T: Temperley, SAM: South AMerica, PO: Pacific Ocean, AO: Atlantic Ocean, SWW: South Westerly Winds, ZW: Zonda Winds, STJ: SubTropical Jet.

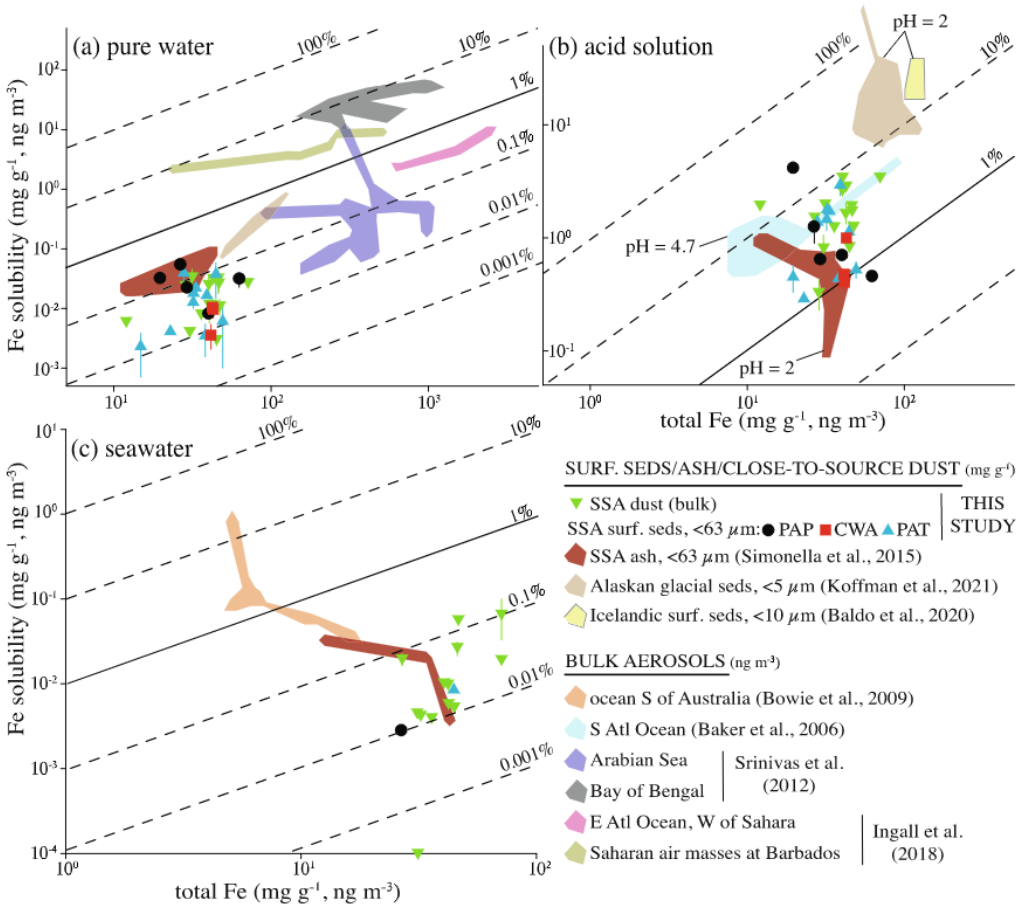

Figure 2. Iron solubility vs. total Fe for dust (bulk) and dust-emitting surface sediments (<63 μm) of southern South America (SSA), based on leaching experiments with (a) pure (i.e., Milli-Q) water for 20 min, (b) pH = 2 nitric acid solution for 2 h, and (c) seawater. Horizontal (a-c) and vertical (a-b) error bars for this study's measurements are 1σ based on three determinations and are smaller than the symbols if not visible. PAP: Puna-Altiplano Plateau, CWA: Central Western Argentina, PAT: Patagonia, Atl: Atlantic.

14. 早中期更新世陆地和海洋温度趋势的解耦合现象

翻译人：夏文月 12231072@mail.sustech.edu.cn

Lu, H., Liu, W., Yang, H., et al. ***Decoupled land and ocean temperature trends in the early‐middle Pleistocene****. Geophysical Research Letters. 2022, 49.*

https://doi.org/10.1029/2022GL099520

摘要：长期陆地温度变化的记录仍旧较短、不连续以及孤立，因此人们普遍认为更新世陆地温度演变应该是跟随海洋温度变化的观点仍未被证实。在本文，我们基于中国黄土高原土壤细菌脂质的分布，提出了过去 3.0 Myr 在亚洲季风区的连续陆地表面温度重建。陆地温度记录表明在更新世期间出现了出乎意料的变暖趋势，和更新世海洋温度的变冷趋势是相反的，从而导致了陆海热量差异的增大。我们提出，先前未被认知的在大部分更新世期间海路热量差异化的增大是一种区域性的气候现象，这个现象为支持更新世东亚夏季风的长期增强提供了一种可能的机制。

ABSTRACT: Record of long-term land temperature changes remains ephemeral, discontinuous, and isolated, thus leaving the common view that Pleistocene land temperature evolution should have followed ocean temperatures unconfirmed. Here, we present a continuous land surface temperature reconstruction in the Asian monsoon region over the past 3.0 Myr based on the distribution of soil bacterial lipids from the Chinese Loess Plateau. The land temperature record indicates an unexpected warming trend over the Pleistocene, which is opposite to the cooling trend in Pleistocene ocean temperatures, resulting in increased land-sea thermal contrast. We propose that the previously unrecognized increase of land-sea thermal contrast during much of the Pleistocene is a regional climate phenomenon that provides a likely mechanism in favor of the long-term enhancement of the Pleistocene East Asian summer monsoon.

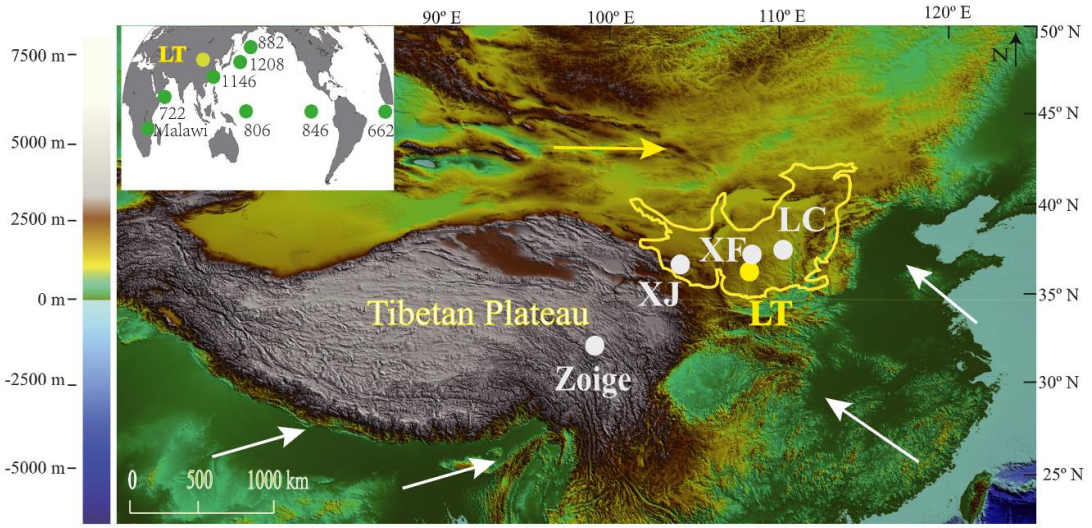

Figure 1. Land relief map of East Asia showing locations of research sites (white circles) near the Lingtai loess-paleosol section (the yellow circle), and other terrestrial and marine (labeled with their ODP number) records used in this study. LC, Luochuan; XF, Xifeng; XJ, Xijin; and LT, Lingtai. Locations of Pleistocene tropical temperature records used in the tropical stack (Herbert et al., 2010) and the two North Pacific records are shown in the inset map. The area enclosed in the yellow line denotes the Chinese Loess Plateau. The yellow (white) arrows indicate the direction of westerlies (summer monsoon) winds. Base map was generated through ArcGIS.

15. 青藏高原全新世水文气候变化：同位素的视角

翻译人：刘宇星 11811211@mail.sustech.edu.cn

Wu D, Ma X, Yuan Z, et al. ***Holocene hydroclimatic variations on the Tibetan Plateau: An isotopic perspective****[J]. Earth-Science Reviews, 2022: 104169.*

https://doi.org/10.1016/j.earscirev.2022.104169

摘要：关于全新世青藏高原水文气候变化的时空格局存在很多争论，特别是在多时间尺度上关注南部和北部地区降水和水汽的偶极格局。现代观测表明，降水中的 $\delta^{18}O$ 是主导青藏高原气候的印度夏季风（ISM）、东亚夏季风（EASM）和西风带大气过程的综合示踪剂。在这里，我们总结和比较了分布在青藏高原的湖泊的 20 个全新世湖泊自生碳酸盐 $\delta^{18}O$ 记录。在仔细考虑温度、蒸发、站位海拔、融水供应和水汽来源的潜在影响后，我们消除了它们对西藏湖泊同位素组成的影响，并认为湖泊 $\delta^{18}O$ 记录的长期变化主要由于水汽来源。青藏高原中西部湖泊沉积物 $\delta^{18}O$ 值自全新世早期以来呈上升趋势，这与高原洞穴记录中 $\delta^{18}O$ 的变化趋势以及该地区季风降水重建的变化相吻合。总体而言，这一证据表明季风对上述地区的影响很大。然而，青藏高原东北部湖泊的 $\delta^{18}O$ 记录在全新世后半期（约 5 ka 之后）显示出下降趋势，突出了该地区不同的水文运行过程，水汽供应有所增强。有人提出，在非季风季节 $\delta^{18}O$ 减少，造成这种变化的原因是来自西风带的水汽贡献增加（例如，来自春季融雪或冻土）。我们认为，亚洲夏季风和西风带的相互作用是全新世青藏高原水文气候变化的主要控制因素，导致了在全新世的千年时间尺度上青藏高原东北部与高原其他地区之间水分变化的偶极模式。

ABSTRACT: There is much debate regarding the temporal and spatial pattern of hydroclimate variations on the Tibetan Plateau during the Holocene, focusing especially on the dipolar pattern of precipitation and moisture between the southern and northern regions, on multiple timescales. Modern observations reveal that the $\delta^{18}O$ in precipitation is an integrated tracer of the atmospheric processes of the Indian summer monsoon (ISM), the East Asian summer monsoon (EASM), and the westerlies, which dominate the climate of the Tibetan Plateau. Here, we summarize and compare 20 Holocene lacustrine authigenic carbonate $\delta^{18}O$ records from lakes distributed across the Tibetan

Plateau. After carefully considering the potential effects of temperature, evaporation, site elevation, meltwater supply, and moisture sources, we eliminate their influences on the isotopic composition of Tibetan lakes, and suggest that the long-term variations of the lacustrine $\delta^{18}O$ records were dominated by the moisture sources. The $\delta^{18}O$ values of the lake sediments in the central and western Tibetan Plateau increased since the early Holocene, which agrees with the trend of $\delta^{18}O$ in speleothem records from the plateau, as well as with the variations of monsoon precipitation reconstructions for the region. Overall, this evidence indicates the substantial influence of the monsoon in the abovementioned regions. However, the $\delta^{18}O$ records from lakes in the northeastern Tibetan Plateau show a decreasing trend during the second half of the Holocene (after ~5 ka), highlighting the operation of a different hydrological process, with enhanced moisture availability, in the regions. It has been suggested that the increased contribution from westerlies-derived moisture in the non- monsoon season, with depleted $\delta^{18}O$ (e.g., from melting snow or frozen soil in spring), is responsible for such variations. We propose that the interplay between the Asian summer monsoon and the westerlies was the major control of the hydroclimatic variations on the Tibetan Plateau during the Holocene, which led to the dipolar pattern of moisture variation between the northeastern Tibetan Plateau and other parts of the plateau, on the multi-millennial timescales during the Holocene.

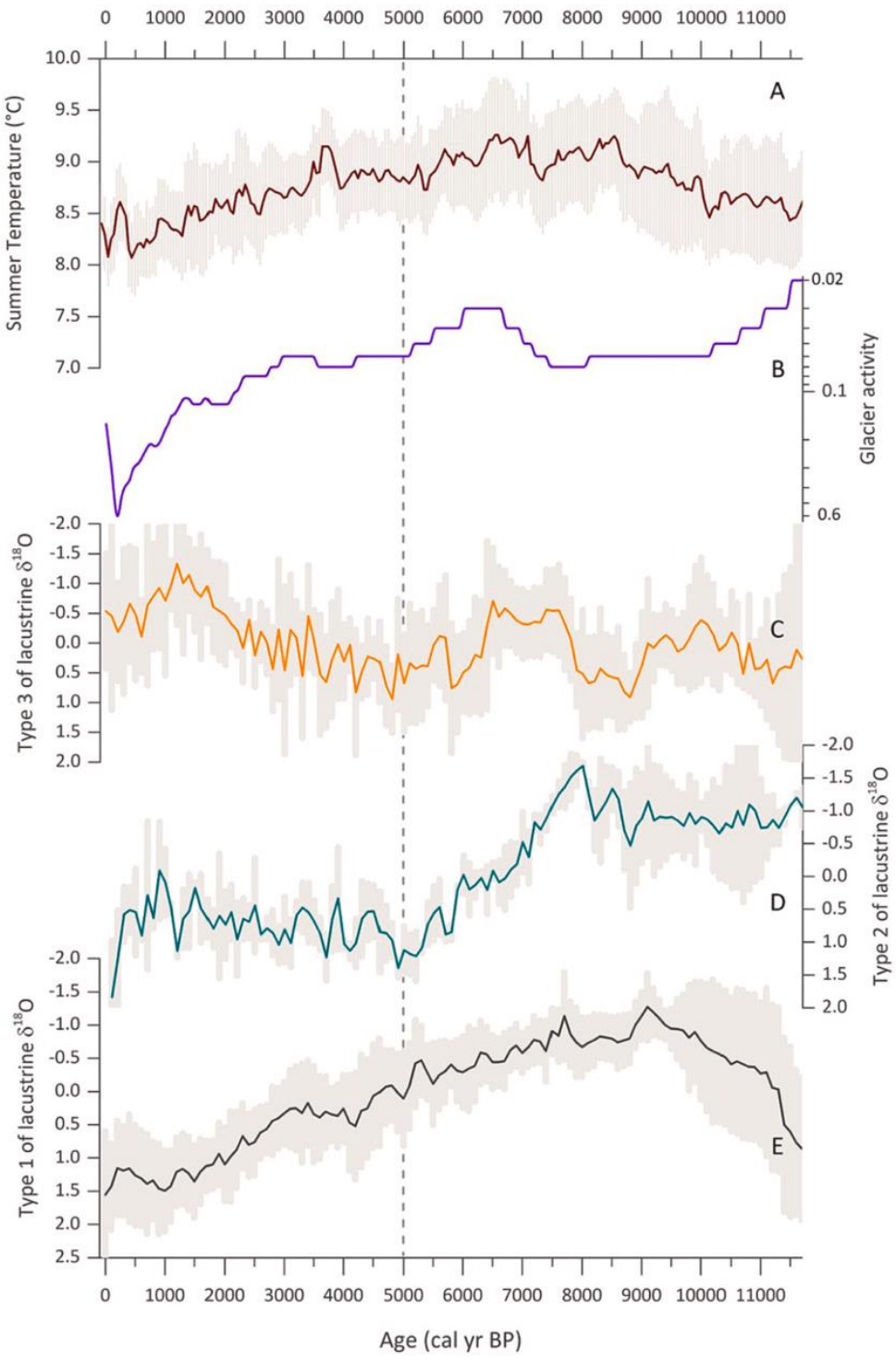

Figure 1. Comparison of the stacked summer temperature reconstruction based on pollen assemblages from 10 lakes and 2 peatland watersheds on the southern, eastern, and northeastern Tibetan Plateau (A; Chen et al., 2020), glacier activity indicated by a probability density plot of moraine ^{10}Be ages; lower values (fewer ages of glacier advances) indicate decreased glacier activity (B; Chen et al., 2020), and three types of lacustrine δ^{18}O records from the Tibetan Plateau (C-E). Types 1–3 are averaged z-score values from δ18O records, each with a 100-year resolution.

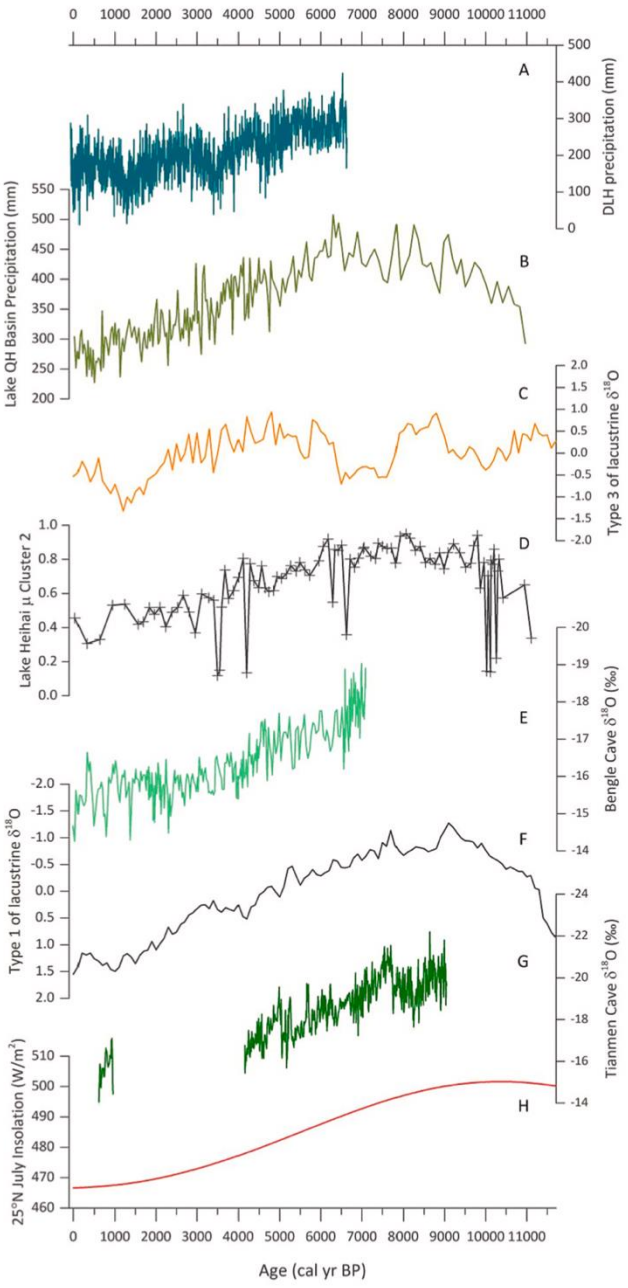

Figure 2. Depth-converted image. Depth-converted mantle reflections, interpreted as the LAB (red) and G-reflection (green). Red dashed line indicates the interpolated depth from 16 Ma to 27 Ma. Best-fitting half-space (solid blue) and plate-cooling (solid black) isotherms are also plotted (1, 53) and have an uncertainty of ±20°C. Results from seismic reflection study across the St. Paul fracture zone are shown by red (top) and green (bottom) stars at 40 Ma and 70 Ma, respectively (13). Dashed gray line with error bars indicates the results from radial anisotropy in the Atlantic Ocean (3). The blue triangles indicate the ensemble of LAB depths observed from previous studies (10) showing widespread LAB depths. Recent results from surface wave tomography (solid dotted blue line) (4) and colocated magnetotelluric experiment (solid dotted brown line) (29) just south of Chain fracture zone have also been plotted. The surface wave tomography and magnetotelluric results have a depth uncertainty of ≥10 to 15 km (4, 29).

16. 500 ka 后暖间冰期东亚夏季风西北缘腾格里沙漠干旱加剧

翻译人：聂美娟 12232216@mail.sustech.edu.cn

Z. Li, F. Wang, C. Luo et al. ***Enhanced drying of the Tengger desert, northwest margin of East Asian summer monsoon during warming interglacials after 500 ka. Quaternary Science Reviews, 293 (2022) 107735***

https://doi.org/10.1016/j.quascirev.2022.107735

摘要：在全球变暖的背景下，干旱半干旱地区面临干旱威胁，但其未来的变化是否干旱存在争议。在干旱沙漠中，中布容事件的高轨道尺度分辨率记录提供了沙漠形成以来的气候模拟，但是目前还没有明确的研究工作。本文对位于东亚夏季风区西北边缘的腾格里沙漠中部最大的湖泊盆地钻探的 122.63 米岩芯进行了年代学和古环境研究。通过综合古地磁分析，在岩心深度 87.5 m 处检测到 Matuyama/Brunhes 边界，根据轨道调谐估计岩心的基础年龄约为 940 ka。通过对岩性、粒度、碳酸盐和总有机碳含量的分析，从而探明沉积相重建古环境演化。根据沉积相确定了 10 个相对湿润的地层，进一步证实了其粒度细、碳酸盐含量高和总有机碳含量高的结果，这些地层普遍发育于间冰期，受过去 940ka 东亚夏季风降水的控制。自过去 500 ka 以来，间冰期气候体系表现为干旱加剧，表现为腾格里沙漠湖泊缩小，沙丘持续流动。我们认为，这种干旱化是由沙漠中大量碎屑物质的供应和中布容事件后在温暖的间冰期出现较高的潜在蒸散发共同造成的。这一研究结果为全球变暖下东亚夏季风边缘沙漠干旱化提供了地质依据。

ABSTRACT: The arid-semiarid regions face drying threats under global warming, but their future changes in terms of drying or not are controversial. High orbital-scale resolution records spanning across the Mid-Brunhes event in the arid deserts provide a climate analogue since the formation of deserts. However, there was no definite work in the deserts so far. Here, we present the results of a chronological and paleo-environmental study of a 122.63 m-long core drilled in the largest lake basin in the central Tengger Desert (northern China), located in the northwestern margin of East Asian Summer Monsoon regions. Following comprehensive paleomagnetism analysis, the

Matuyama/Brunhes boundary was detected at a core depth of 87.5 m, and the basal age of the core is estimated at ~940 ka based on orbital tuning. The lithology, grain size, carbonate and total organic carbon content were analyzed to examine the sedi-mentary facies and reconstruct the paleoenvironmental evolution. Ten relatively humid layers were identified by sedimentary facies, further results confirmed by fine grain size, high carbonate, and total organic carbon content, which generally developed during interglacial and were controlled by the East Asian summer monsoon precipitation during the past 940 ka. Since ~500 ka, the interglacial climate regime displayed an intensified aridification manifested as shrinking lakes and persistent mobile dunes in the Tengger Desert. We argue that this aridification was caused by the combination of a massive supply of clastic material for the desert and the occurrence of higher potential evapotranspiration during warmer interglacials after the Mid-Brunhes Event. This research finding provides geological evidence for the aridification of the deserts in the East Asian Summer Monsoon margin under global warming.

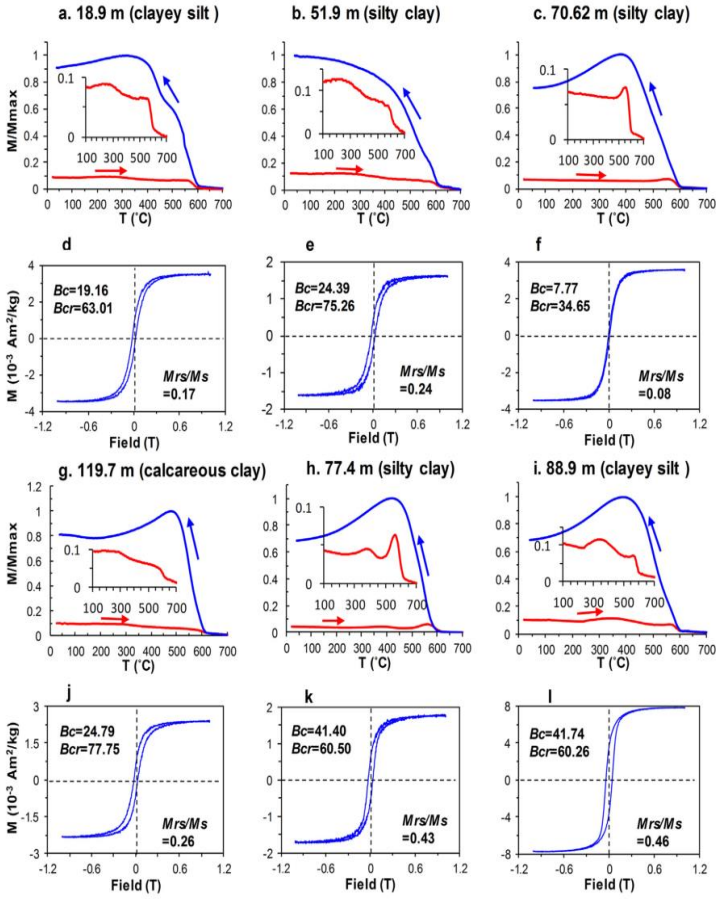

Figure 1. Temperature-dependent magnetic susceptibility (χ -T) curves and hysteresis loops for representative samples at different depths from drill core WEDP06. (**a-c**, **g-i**) χ -T curves and their zoom-ins of heating curves. The red/blue line indicates the heating/cooling. (**d-f, j-l**) Hysteresis loops after 70% paramagnetic correction.

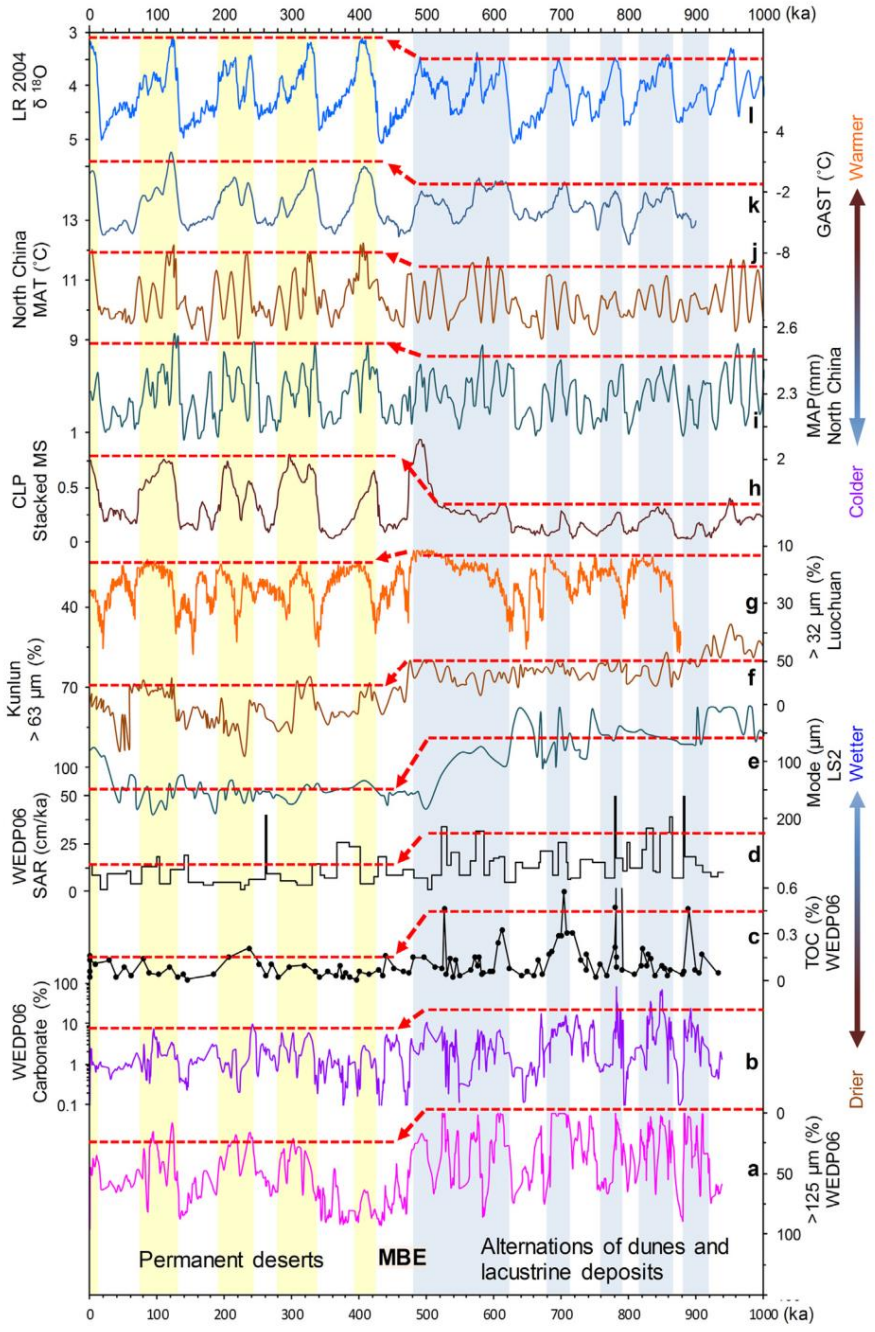

Figure 2. Enhanced drying around ~500 ka in arid northwest China, and comparison with CLP and global paleoclimatic records. (**a-d**) >125 mm grain size fraction, carbonate content,TOC content and SAR from WEDP06. SAR was calculated based on the tie points of tuning. (**e**) Mode size of LS2 core in Lop Nur (Liu et al., 2020). (**f**) > 32 mm fraction average values of loess core in West Kunlun Mountains (Fang et al., 2020). (**g**) > 32 mm grainesize fraction of the Luochuan loess section (Hao et al., 2012). (**h**) Stacked magnetic susceptibility record of Chinese loess (Sun et al., 2006). (**i**) Simulated mean annual precipitation (MAP) and (**j**) mean annual temperature (MAT) over northern China (Sun et al., 2019). (**k**) Simulated global average surface temperatures (GAST, Snyder, 2016). (**l**) Benthic d18O LR04 (Lisiecki and Raymo, 2005).